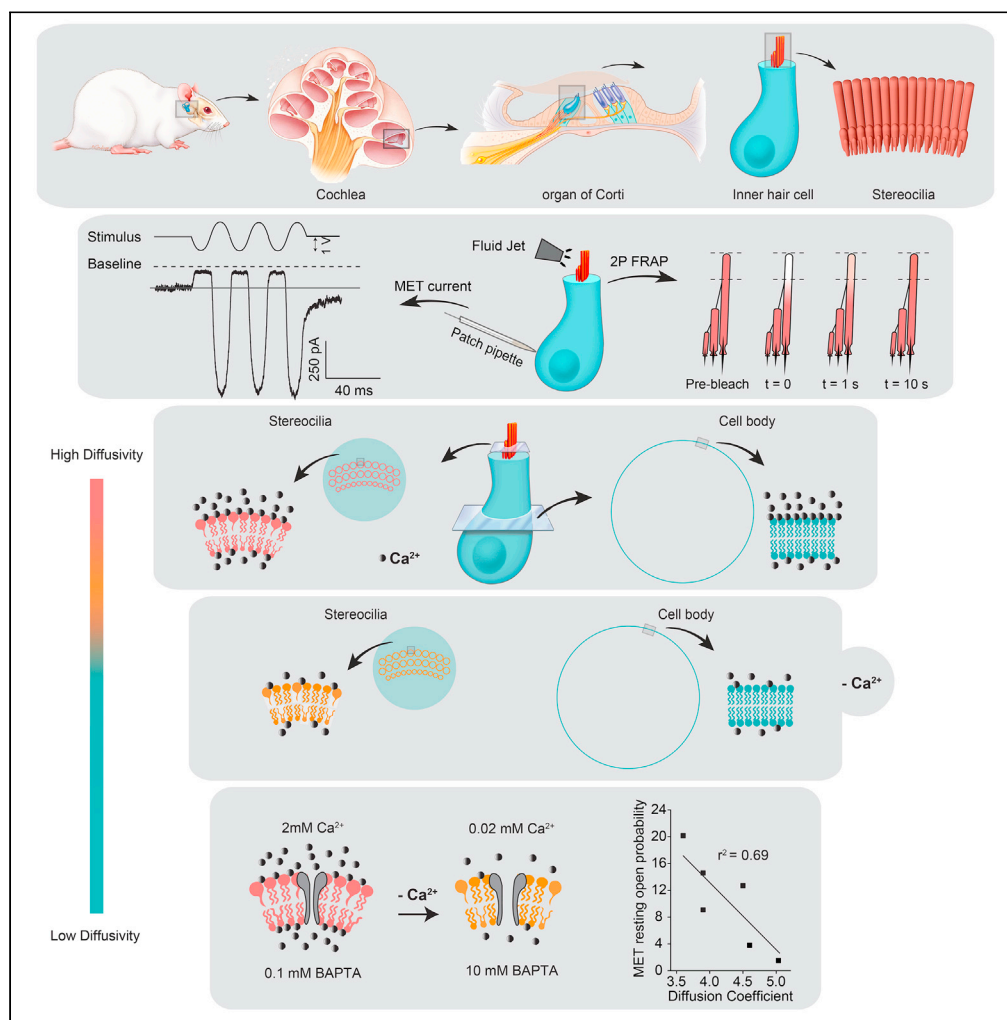CellPress
OPEN ACCESS

Article

Rat Auditory Inner Hair Cell Mechanotransduction and Stereociliary Membrane Diffusivity Are Similarly Modulated by Calcium

Shefin S. George,
Charles R. Steele,
Anthony J. Ricci

aricci@stanford.edu

HIGHLIGHTS

Stereocilia membranes are highly diffusive as compared to the cell body membrane

Stereocilia membrane diffusivity varies with internal and external calcium levels

MET channel resting open probability increases as membrane diffusivity decreases

Article

Rat Auditory Inner Hair Cell Mechanotransduction and Stereociliary Membrane Diffusivity Are Similarly Modulated by Calcium

Shefin S. George,[1] Charles R. Steele,[2] and Anthony J. Ricci[1,3,4,*]

SUMMARY

The lipid bilayer plays a pivotal role in force transmission to many mechanically-gated channels. We developed the technology to monitor membrane diffusivity in order to test the hypothesis positing that Ca^{2+} regulates open probability (P_o) of cochlear hair cell mechanotransduction (MET) channels via the plasma membrane. The stereociliary membrane was more diffusive (9x) than the basolateral membrane. Elevating intracellular Ca^{2+} buffering or lowering extracellular Ca^{2+} reduced stereociliary diffusivity and increased MET P_o. In contrast, prolonged depolarization increased stereociliary diffusivity and reduced MET P_o. No comparable effects were noted for soma measurements. Although MET channels are located in the shorter stereocilia rows, both rows had similar baseline diffusivity and showed similar responses to Ca^{2+} manipulations and MET channel blocks, suggesting that diffusivity is independent of MET. Together, these data suggest that the stereociliary membrane is a component of a calcium-modulated viscoelastic-like element regulating hair cell mechanotransduction.

INTRODUCTION

Mechanotransduction (MET) is a key step in many sensory processes, including touch, proprioception, pain, osmoregulation, cell adhesion, balance, and hearing. A common feature to each of these is the activation of mechanosensitive ion channels. In principle, force gating of mechanosensitive ion channels can occur through the lipid bilayer ("force-from-lipids" principle) or through tether-forming proteins that connect the channel to the cytoskeletal and/or extracellular matrix ("force-from-filament" model) to translate mechanical stimulus into electrical or biochemical signals (Ursell and Blount, 2008; Martinac and Poole, 2018). These mechanisms are not mutually exclusive, and the lipid bilayer can play a role in force transmission in both scenarios.

The lipid bilayer is indirectly implicated in modulating cochlear hair cell MET. GsMTx4, a lipid-mediated stretch-activated channel modifier (Suchyna et al., 2000; Bowman et al., 2007), shifts the MET activation curve rightward, decreasing the resting open probability (P_o) of MET channel, and inhibits the leftward shift induced by reducing extracellular divalent ions and membrane depolarization (Peng et al., 2016). Increasing intracellular Ca^{2+} buffering also shifts the activation curve leftward, increasing the resting P_o independent of the extracellular effects. PIP2, an endogenous lipid, modulates MET channel conductance, open probability, and kinetics (Hirono et al., 2004; Effertz et al., 2017; Cunningham et al., 2020). And finally, computational models support a role for the lipid bilayer in shaping the force exerted on hair cell MET channels (Powers et al., 2012, 2014; Gianoli et al., 2017). Present work directly assesses membrane diffusivity, one component of membrane mechanical properties.

Hair cells detect mechanical stimuli via displacement of their sensory hair bundle. The apically located hair bundle comprises an array of stereocilia, actin-filled microvilli, that increase in height in a staircase-like manner. An extracellular tether, the tip link, connects stereocilia columns such that deflection toward the tallest stereocilia row pulls the tip link (Pickles et al., 1984), exerting force that is transmitted to MET channels located at the top of the shorter stereocilia (Beurg et al., 2009). MET channels are mechanically coupled to the tip link through several membrane-spanning proteins and the lipid bilayer and likely also with proteins spanning from the plasma membrane to the cytoskeleton (Gillespie and Müller, 2009; Peng et al., 2011). The upper tip link is similarly coupled both to the membrane and cytoskeleton through

[1]Department of Otolaryngology-Head and Neck Surgery, School of Medicine, Stanford University, 240 Pasteur Drive, Stanford, CA 94305, USA

[2]Department of Mechanical Engineering, Building 520, 440 Escondido Mall, Stanford University, CA 94305, USA

[3]Department of Molecular and Cellular Physiology, School of Medicine, Stanford University, 291 Campus Drive, Stanford, CA 94305, USA

[4]Lead Contact

*Correspondence: aricci@stanford.edu

https://doi.org/10.1016/j.isci.2020.101773

a variety of proteins, likely including myosin molecules. How the lipid bilayer influences mechanical coupling between these molecules and thus modulates force transmission to the MET channel is a focus of the present work.

One method for monitoring membrane properties uses FRAP (fluorescence recovery after photobleaching) to measure lateral diffusivity of fluorescent particles as a measure of membrane properties. Lateral fluorescent particle diffusivity, which we refer to as membrane diffusivity for simplicity, is influenced by factors such as the lipid and protein composition, membrane order (lipid packing efficiency), membrane curvature, membrane tension (stress in the plane of the membrane), and hydrophobic thickness (Butler et al., 2001; Haidekker et al., 2001; Blood et al., 2005; Reddy et al., 2012). FRAP provides an average across a large volume of membrane (optically limited) over a relatively slow time course. FRAP does not provide information regarding fast changes in membrane properties or nanodomains created by individual proteins, but measurements can be influenced by underlying specializations. Changes in these membrane properties might alter diffusivity and indirectly affect membrane protein structure and function (Tillman and Cascio, 2003). Diffusivity is inversely related to membrane viscosity, but the specific relationship is complex and dependent on many of the properties described above.

We explored stereociliary membrane diffusivity using two-photon FRAP of the lipid probe di-3-ANEPPDHQ under conditions known to alter MET channel resting P_o in rat inner hair cells (IHCs) and their stereocilia. We found that the stereociliary membrane is about nine times more diffusive than the IHC soma, consistent with previous findings (Boutet de Monvel et al., 2006). Unlike the soma, stereociliary diffusivity is sensitive to Ca^{2+} and voltage, yet independent of MET channel activity. Our data support a mechanism whereby the stereociliary membrane diffusivity and MET channel P_o are co-modulated such that increases in diffusivity are paralleled by decreases in MET channel P_o.

RESULTS

One-Dimensional Diffusion in the Stereociliary Membrane

Two-photon FRAP was used to evaluate membrane diffusivity in rat apical IHCs. The tallest (row 1) and middle (row 2) rows of the sensory hair bundle were evaluated using the membrane dye, di-3-ANEPPDHQ, as illustrated in Figures 1A–1D. The laser beam was focused at the top of a stereocilium which allowed for the average fluorescence intensity of a 1.9 μm long region (axial resolution of our optical system) of that stereocilium to be monitored over time. Figure 1C shows a set of stereocilia before and after photobleaching, with the bleached, reference, and background regions highlighted. Following background subtraction and photobleaching correction, a normalized fluorescence intensity vs time plot (FRAP curve) was generated with t = 0 representing the first post-bleach measurement (Figure 1E). To estimate the diffusion coefficient D, the FRAP curve was fitted with a stereocilia-specific one-dimensional diffusion model (Figure 1E). Details of FRAP parameters and diffusion models are presented in Methods and Figures S1–S3. The filled appearance of the stereocilia initially questioned dye localization to the plasma membrane. Further investigations revealed "excitation photoselection effect" (Parasassi et al., 1997; Bagatolli, 2006) that was corrected with a half-wave plate as illustrated in Figure S3. D values were similar with or without the half-wave plate rotation, confirming diffusion was only occurring through the membrane (Figure S3H).

Stereociliary Membrane Is Highly Diffusive Compared to the Soma

We compared FRAP measurements from the stereocilia to those of the IHC's soma, near the top of the nucleus, as a control for stereociliary specific behavior. Figure 1F presents average FRAP curves from the soma and both rows of stereocilia illustrating differences in recovery time courses. The soma recovered fastest while the row 1 stereocilia recovered slowest. In agreement with the FRAP curves, the time constants were significantly faster (*t* test, p < 0.001) for the soma, 0.2 ± 0.05 s (n = 8 cells) compared to the row 2 stereocilia, 1.1 ± 0.2 s (n = 43 cilia), which are faster again (*t* test, p < 0.001) than the row 1 stereocilia, 4.5 ± 1 s (n = 21 cilia) (Figure 1G). However, the time constants of recovery are greatly influenced by the geometry of the investigated system and the bleach extent. Thus, it is critical to develop a morphologically accurate model to correct for these parameters in order to extract a biologically relevant diffusion constant (see Supplemental Information). The estimated diffusion constants between stereociliary rows were not significantly different from each other, with values of 5.1 ± 1.1 μm^2/s for row 1 stereocilia and 5.6 ± 0.8 μm^2/s for row 2 stereocilia (Figure 1H). However, the stereociliary diffusion constant was about nine times greater than that of the soma of 0.58 ± 0.13 μm^2/s (Figure 1H). These results are in agreement with the previous finding of Boutet De Monvel et al. (2006) who report larger diffusion constants for outer hair cell (OHC) stereocilia
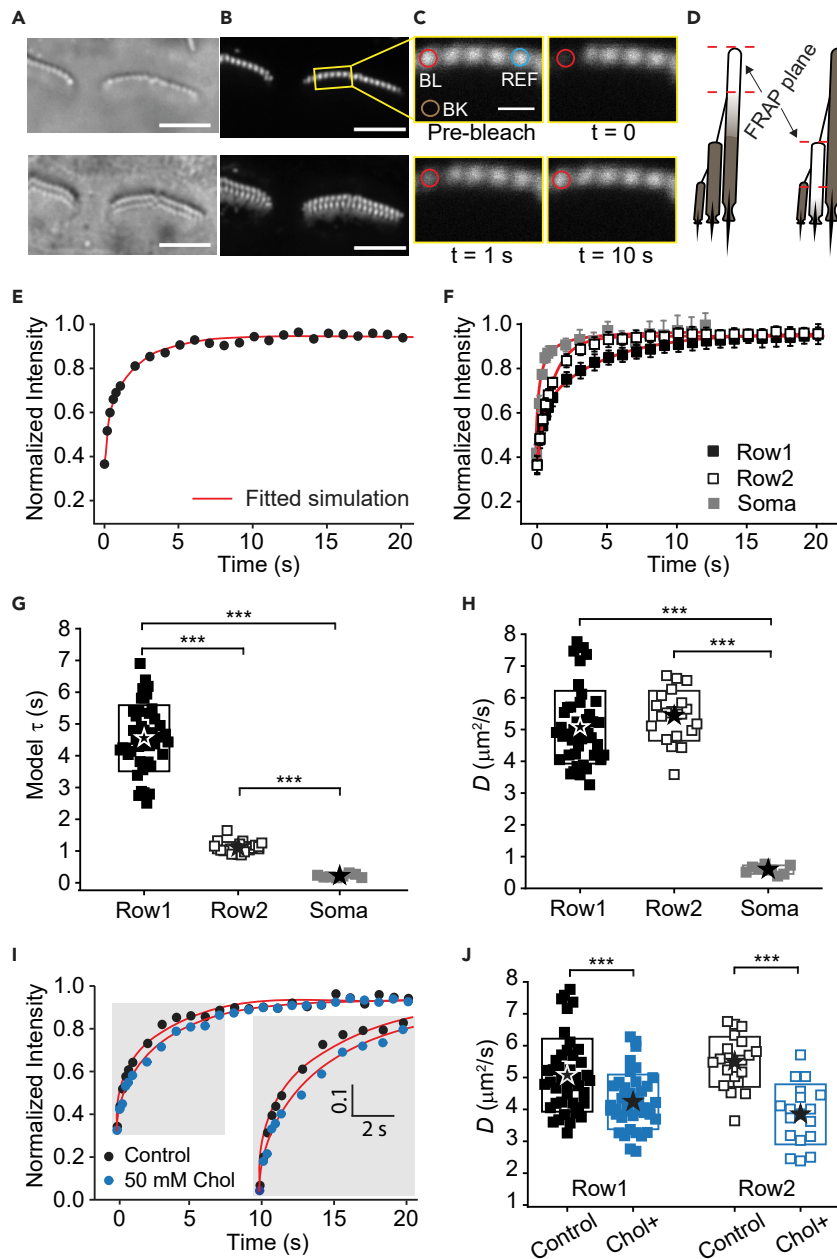
Figure 1. Setup of Two-Photon FRAP of Membrane Dye di-3-ANEPPDHQ in IHC Stereocilia

(A and B) (A) Bright field and (B) two-photon sections of the same IHC bundles stained with di-3-ANEPPDHQ and oriented vertically, focused at the tip of the row 1 (top) and row 2 (bottom) stereocilia. Scale bar represents 5 μm.

(C) Representative FRAP experiment on the row 1 stereocilia with t = 0 indicating the first image taken post-bleaching. The red, blue, and brown circles define the bleached (BL), reference (REF), and background (BK) regions, respectively. Scale bar represents 1 μm.

(D) Depiction of an IHC bundle with red dashed lines indicating the approximate position of the focal plane at the tip of the row 1 and row 2 stereocilia for FRAP experiments. Only one stereocilia was bleached at a time. The gradient filling indicates the degree of bleaching with white representing the highest degree of bleaching.

(E) The experimental FRAP curve is fitted with a one-dimensional diffusion model to estimate the diffusion constant D, yielding a value of 4.6 μm²/s with a fitting error of 1.2%.

(F) The average FRAP curves (mean ± SD) and the corresponding fitted curves (red trace) for the row 1 stereocilia (n = 43, black filled squares), row 2 stereocilia (n = 21, black unfilled squares), and the cell body (n = 8, gray filled squares).

Figure 1. *Continued*

(G) Time constant τ derived from fitting the data, showing significantly faster recovery for the cell body than the stereocilia. Row 1 recovery was significantly faster than that of row 2 (t test, p < 0.001).

(H) Diffusion constants extracted from the model were similar for row 1 and row 2 stereocilia and were significantly larger than those of the soma (t test, p < 0.001).

(I) FRAP data points and fitted curves comparing control stereocilia to stereocilia treated with 50 mM water-soluble cholesterol complex to load cholesterol into the membrane. The estimated D values for the given examples are 5 μm^2/s (fitting error = 2.2%) for the control stereocilia and 3.6 μm^2/s (fitting error = 1.7%) for the cholesterol loaded stereocilia.

(J) Cholesterol loading resulted in significant reduction in the diffusivity in both row 1 and row 2 stereocilia (t test, p < 0.001).

Boxes in (G), (H), and (J) represent the SD, and the star symbol indicates the mean. Each data point corresponds to a stereocilium (for row1 and row2) or a cell (for soma). ***p < 0.001.

compared to soma (Table S1). Despite experimental (i.e., bleach extent, bleach time, dye selection) and morphological differences between our observations and those of Boutet De Monvel et al. (2006), resulting in recovery time constants differing by ~25 fold, the diffusion constants of the soma are comparable and smaller than those of the stereocilia (Figure S2E). The marked difference between stereocilia and soma might imply a functional relevance to the diffusivity.

FRAP Sensitivity

FRAP sensitivity was evaluated by increasing membrane cholesterol levels, a manipulation previously shown to reduce membrane diffusivity (Nguyen and Brownell, 1998; Organ and Raphael, 2009). Figures 1I and 1J show that cholesterol addition slowed the time course of FRAP curves compared to control, with corresponding reductions in the diffusion constant for both stereociliary rows (t test, p < 0.001), from 5.1 $\pm$ 1.1 μm^2/s to 4.2 $\pm$ 0.8 μm^2/s for row 1 stereocilia and 5.6 $\pm$ 0.8 μm^2/s to 3.8 $\pm$ 0.9 μm^2/s for row 2 stereocilia. Similarly, the time constant showed significant increases (t test, p < 0.001) with cholesterol addition in both stereociliary rows, with no significant effect (t test, p > 0.2) on the mobile fraction of recovery (Figure S4). Thus, the membrane enrichment with cholesterol decreases membrane fluidity, consistent with previous reports (Owen, 2015; Ayee and Levitan, 2016). This result further demonstrates that FRAP measurement implemented at the level of individual stereocilium could detect the reduction in diffusivity of di-3-ANEPPDHQ in the stereocilia membrane. And finally, the cholesterol-induced change of ~25% is modest compared to the difference between soma and stereocilia (x9), suggesting additional factors are needed to explain the differences between soma and stereocilia.

Effect of Internal Ca^{2+} Buffering on Membrane Diffusivity

The lipid membrane is implicated in modulating the resting P_o of the hair cell MET channel (Peng et al., 2016; Effertz et al., 2017). Hypothesizing that the viscoelastic properties of the stereocilia membrane impact MET channel properties, we investigated lipid membrane diffusivity as a first step in probing membrane mechanics, under conditions that alter MET channel resting P_o. As diffusivity is an indication of viscosity, any correlation between diffusivity and MET channel resting P_o can only suggest a common regulatory site for the two processes as viscosity effects can only manifest themselves in a non-steady state condition, i.e., during stimulation.

Elevated internal Ca^{2+} buffering increases MET channel resting P_o (Crawford et al., 1991; Ricci and Fettiplace, 1997). To examine the effect of internal Ca^{2+} buffering on the stereocilia membrane diffusivity, we compared FRAP results from the stereocilia of cells patched with 0.1 mM BAPTA (1,2-bis(o-aminophenoxy)ethane-N,N,N',N'-tetra-acetic acid) and 10 mM BAPTA in the internal solution. Increasing internal Ca^{2+} buffering from 0.1 mM BAPTA to 10 mM BAPTA with a holding potential of −84 mV increased resting P_o significantly (t test, p < 0.001) from 3.8 $\pm$ 1.4% (n = 65 cells) to 14.6 $\pm$ 4.6% (n = 47 cells) (Figures 2A and 2B), similar to other reports (Fettiplace, 1992; Ricci and Fettiplace, 1997; Peng et al., 2013).

Figures 2C and 2D summarize average FRAP curves measured across the two rows of stereocilia comparing 0.1 mM BAPTA to 10 mM BAPTA with the superimposed model fits for each data set. There is a small but distinct slowing of recovery with higher BAPTA concentrations, similar in scale to that observed with elevating cholesterol. Both stereociliary rows show a similar slowing of recovery with elevated BAPTA. The diffusion constant (Figure 2E) similarly suggests that both stereociliary rows are sensitive to BAPTA concentration in that diffusivity in 10 mM BAPTA (3.9 $\pm$ 0.8 μm^2/s for row 1 and 3.9 $\pm$ 0.5 μm^2/s for row 2) and is significantly reduced (t test, p < 0.001) as compared to 0.1 mM BAPTA (4.8 $\pm$ 1.1 μm^2/s for row
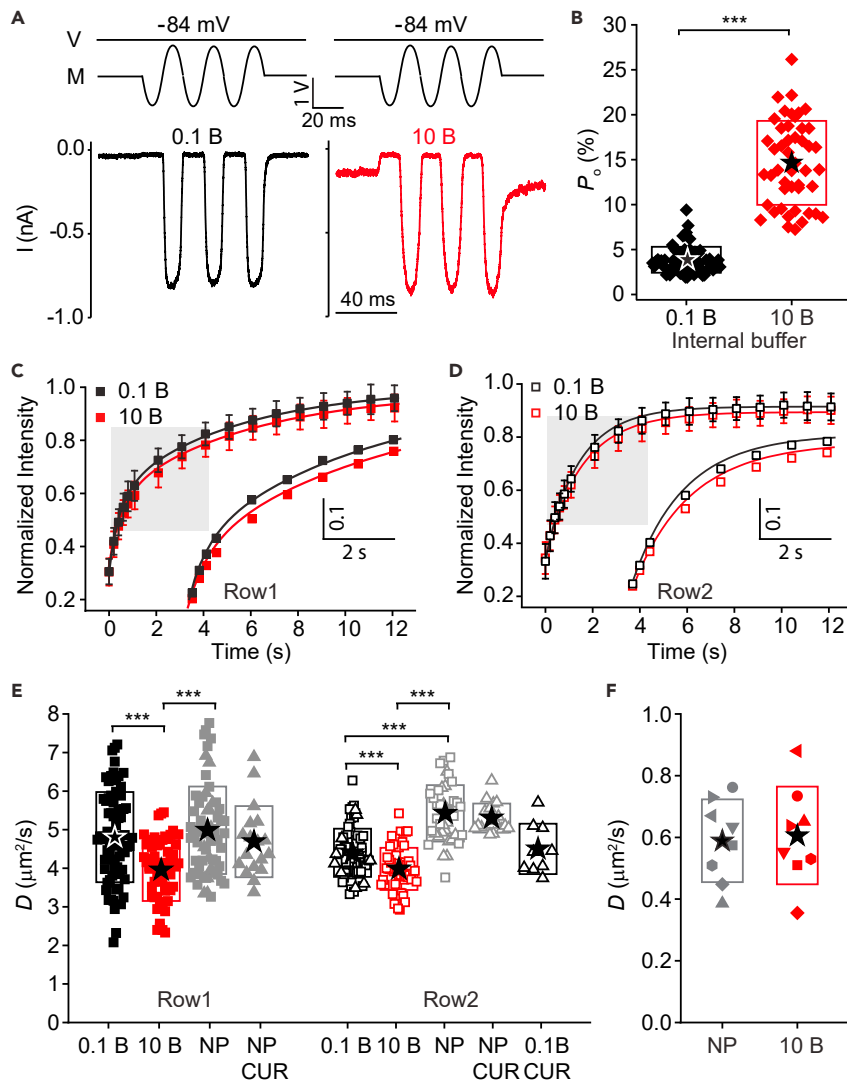
Figure 2. Internal Ca^{2+} Buffering Reduces Membrane Diffusivity of the Stereocilia

(A) Voltage-clamped (V) MET current responses of IHCs to fluid jet sinusoidal stimulus (M) with 0.1 mM BAPTA (black) and 10 mM BAPTA (red) internal solutions, with a holding potential of −84 mV.

(B) Summary box plots for the resting open probability (P_o) measured for 0.1 mM BAPTA (n = 65 cells) and 10 mM BAPTA (n = 47 cells) internal solutions. Each data point corresponds to a cell.

(C and D) Average FRAP data points (mean ± SD) and fitted curves from the row 1 (C) and row 2 (D) stereocilia comparing 0.1 and 10 mM BAPTA internal solutions. Insets show slower FRAP curves with 10 mM compared to 0.1 mM BAPTA internal solutions.

(E) Summary box plots show that the diffusion constant was significantly lower with 10 compared to 0.1 mM BAPTA for both stereocilia rows (t test, p < 0.001). There was a significant reduction in diffusivity (t test, p < 0.001) of row 2 with 0.1 mM BAPTA compared to unpatched cells. Also, application of 1 mM curare had no effect on the diffusivity of row 1 and row 2 with and without patching (t test, p < 0.001). Each data point corresponds to a stereocilium.

(F) Summary of diffusion constants from the soma shows no significant difference between unpatched cells and patched with 10 mM BAPTA internal solution. Different symbols correspond to different cells.

Boxes in (B), (E), and (F) represent the SD, and the star symbol indicates the mean. 0.1 B, 0.1 mM BAPTA; 10 B, 10 mM BAPTA; NP, not patched; NP CUR, not patched and treated externally with 1 mM curare; 0.1B CUR, patched with 0.1 mM BAPTA internal and treated externally with 1 mM curare. ***p < 0.001.

1 and 4.4 ± 0.6 μm^2/s for row 2). The time constants also showed a significant increase (t test, p < 0.001) with elevated internal Ca^{2+} buffering in both stereociliary rows, with no effect on the mobile fraction of recovery (Figure S5).

Role of MET Channel in Modulating Diffusivity

We observed a difference in D values between rows when comparing hair cells prior to obtaining a whole-cell recording to those with 0.1 mM BAPTA internal solution, with row 2 having a statistically significant reduction in D (t test, p < 0.001) while row 1 remained unaffected (Figure 2E). One possible interpretation of this difference is that row 2 has a higher Ca^{2+} concentration because of the functional MET channels located in them, making row 2 more sensitive to BAPTA. Similarly, the reduced relative change between 0.1 and 10 mM BAPTA for row 2 (19% in row 1 and 11% in row 2) may reflect local buffer saturation in row 2 with 0.1 mM BAPTA because of open MET channels in row 2. To determine whether the difference between the 0.1 mm BAPTA and the non-patched cell was due to changes in MET channel P_o, we applied curare (1 mM) externally to non-patched hair bundles to block the MET channels (Glowatzki et al., 1997; Farris et al., 2004; Kirkwood et al., 2017). Curare had no effect on membrane diffusivity of stereocilia, arguing MET channels were not driving the difference. We also tested the row 2 membrane sensitivity to Ca^{2+} entry through MET channels by applying curare after obtaining whole-cell mode (with 0.1 mM BAPTA internally); curare addition again had no effect on the enhanced BAPTA sensitivity of row 2, further arguing that adjustments to MET channel P_o were not responsible for changes in diffusivity. The 10 mM BAPTA condition similarly effects both stereociliary rows relative to non-patched cells (24% in row 1 and 30% in row 2), potentially by removing Ca^{2+} away from the lipid bilayer and altering lipid packing (Ito and Ohnishi, 1974; Melcrova et al., 2016). Thus, we find stereociliary membrane diffusivity to be sensitive to internal Ca^{2+} buffer but to be independent of MET channel activity.

It is possible that membranes are simply sensitive to Ca^{2+} buffers, specifically BAPTA, and that stereocilia are not unique in this property. We compared IHC basolateral membrane sensitivity to Ca^{2+} buffers as a test of this hypothesis and found that unlike stereocilia, the basolateral membrane diffusivity was unaffected by 10 mM BAPTA (Figure 2F). Therefore, stereocilia appear to be uniquely sensitive to Ca^{2+} buffering. It remains plausible that a common underlying mechanism influences MET channel P_o and membrane diffusivity and that MET channel activity does not impact this underlying mechanism.

Effect of Extracellular Ca^{2+} on Membrane Diffusivity

Lowering extracellular Ca^{2+} increases MET channel resting P_o (Crawford et al., 1991; Peng et al., 2016; Effertz et al., 2017) and its effect on P_o is blocked by GsMTx4, a compound that interferes with force transmission through the bilayer to MET channels (Suchyna et al., 2000; Bowman et al., 2007; Peng et al., 2016). We investigated the effect of extracellular Ca^{2+} on the diffusivity of di-3-ANEPPDHQ with 0.1 mM BAPTA or 10 mM BAPTA as the internal Ca^{2+} buffer. Lowering extracellular Ca^{2+} from 2 to 0.02 mM increased MET channel resting P_o (Figures 3A and 3B) from 3.1 $\pm$ 1.0% to 9.1 $\pm$ 6.2% with 0.1 mM BAPTA (paired t test, p < 0.001) and from 12.7 $\pm$ 4% to 20.2 $\pm$ 10.3% with 10 mM BAPTA (paired t test, p < 0.01). Lowering extracellular Ca^{2+} to 20 μM increases (paired t test, p < 0.001) the maximum MET current (Figure 3C), from 0.7 $\pm$ 0.1 nA to 1.2 $\pm$ 0.2 nA with 0.1 mM BAPTA internal solution and from 0.7 $\pm$ 0.1 nA to 1.1 $\pm$ 0.2 nA with 10 mM BAPTA internal solution, a result due to removal of Ca^{2+} block from the MET channel (Crawford et al., 1991; Ricci and Fettiplace, 1998). FRAP measurements were obtained after observing the reported increase in resting P_o and maximum MET current which ensured reliable hair bundle perfusion and equilibration of the 20 μM Ca^{2+}. As this experiment requires repeated FRAP measurements over time, we first demonstrate that the FRAP values are stable over the duration of the experimental time (Figure S6A). Lowering extracellular Ca^{2+} results in slower recovery in the stereocilia for both 0.1 and 10 mM BAPTA internal solutions as indicated by average FRAP curves (Figures 3D and 3G). The diffusion constants of the stereociliary membrane were significantly decreased in both rows (Figures 3E and 3H) in the presence of low extracellular Ca^{2+}, from 5.7 $\pm$ 1.1 μm^2/s to 4.2 $\pm$ 1.4 μm^2/s (paired t test, p < 0.01) and 4.4 $\pm$ 0.8 μm^2/s to 3.6 $\pm$ 0.8 μm^2/s (paired t test, p < 0.05) for the row 1 and row 2 stereocilia, respectively, with 0.1 mM BAPTA internal solution. With 10 mM BAPTA internal solution, the diffusivity reduced from 4.6 $\pm$ 0.8 μm^2/s to 3.4 $\pm$ 0.8 μm^2/s (paired t test, p < 0.001) and 4.5 $\pm$ 0.8 μm^2/s to 3.8 $\pm$ 0.7 μm^2/s (paired t test, p < 0.01) for row 1 and row 2 stereocilia, respectively. Both internal solutions produced similar shifts in the diffusion constant in both rows of stereocilia (Figures 3F and 3I), suggesting that the effector site was external, similar to a previous report on MET channel P_o (Peng et al., 2013).

Similarly, the time constants showed significant increase (paired t test, p < 0.001) with low extracellular Ca^{2+} in both rows of stereocilia, with no significant effect on the mobile fraction of recovery (Figures S6B–S6D). The time course of recovery upon returning the extracellular Ca^{2+} back to 2 mM appears slower than we accounted for in our measurements such that some stereocilia recovered to a lesser degree than the original measurements. The recovery was not statistically different than the control, and there was no buffer concentration or row-specific
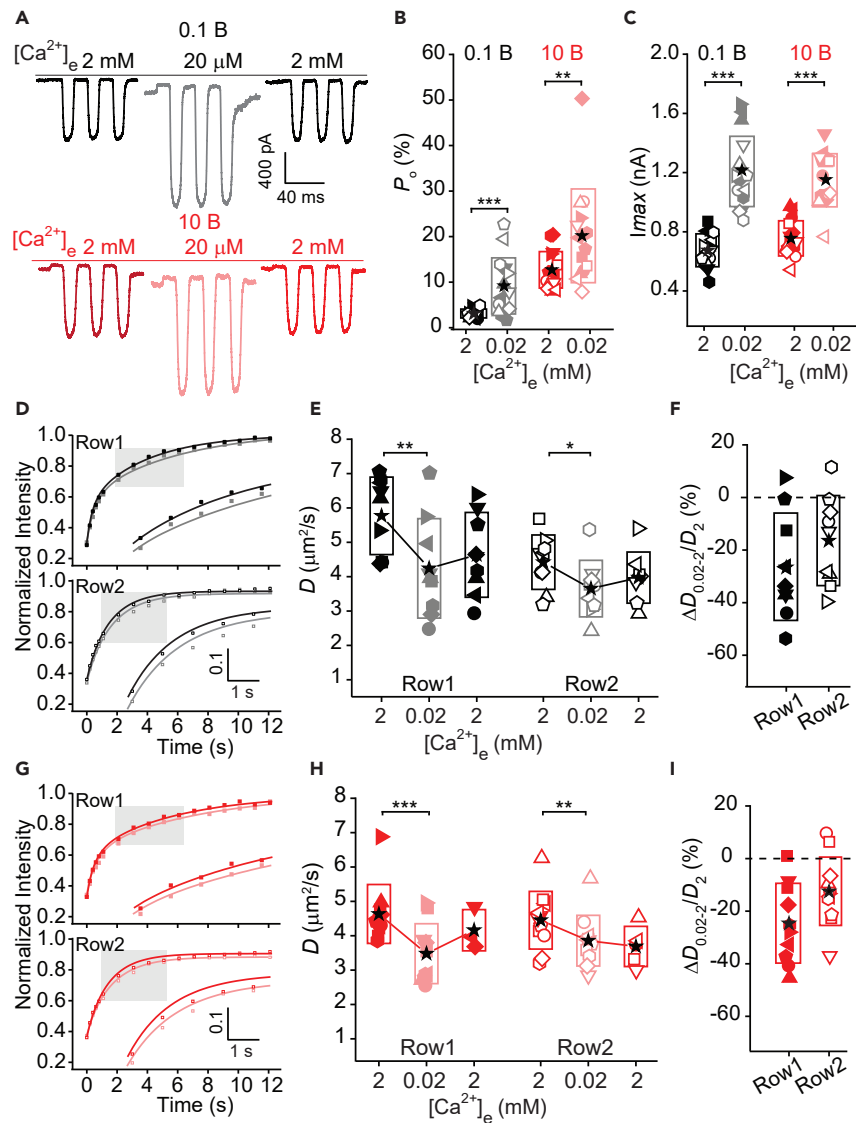
Figure 3. Lowering External Ca²⁺ Reduces Stereociliary Membrane Diffusivity

(A) Representative current responses to sinusoidal fluid jet stimulation from IHCs before, during, and after application of 0.02 mM Ca^{2+} external solution, with 0.1 mM BAPTA internal (top) and 10 mM BAPTA internal (bottom). Note the increase in baseline current and MET current in the presence of low Ca^{2+} external.

(B and C) (B) Resting P_o and (C) peak MET current $Imax$ increases significantly when the external Ca^{2+} concentration is reduced from 2 to 0.02 mM (paired t test, $p < 0.01$). Each symbol indicates a cell for a given internal solution.

(D) and (G) Average FRAP data points and fitted curves comparing 2 mM (black traces for 0.1 mM BAPTA internal and red traces for 10 mM BAPTA internal) with 0.02 mM Ca^{2+} external (gray traces for 0.1 mM BAPTA internal and light red traces for 10 mM BAPTA internal) for row 1 and row 2 stereocilia.

(E) and (H) Summary box plots of diffusion constants with 0.1 mM BAPTA internal solution (E, black and grey symbols) and 10 mM BAPTA internal solution (H, red and light red symbols) show a significant reduction in diffusivity in the presence of 0.02 mM Ca^{2+} external irrespective of the internal solution and the row of stereocilia (paired t test, $p < 0.05$). Each symbol in a graph corresponds to a bundle.

(F) and (I) The fractional decrease in D values when the external Ca^{2+} is reduced from 2 to 0.02 mM was not significantly different between the internal solutions i.e., 0.1 mM BAPTA (F) and 10 mM BAPTA (I) and the rows of stereocilia.

Boxes represent the SDs, and the star symbol indicates the mean. 0.1 B, 0.1 mM BAPTA; 10 B, 10 mM BAPTA. *$p < 0.05$, **$p < 0.01$, ***$p < 0.001$.

differences in the recovery measurement. We did not compare the stereociliary membrane to that of the soma in low external Ca^{2+} due to the inability to reproducibly expose the basolateral hair cell membrane to low Ca^{2+} solution using the apical perfusion pipette in the semi-intact epithelial preparation.

Our results indicate that extracellular Ca^{2+} modulation of membrane diffusivity is independent of the internal buffer, as the fractional changes in diffusivity were unaffected (t test, p > 0.05) by the internal buffer. Data support the idea of extracellular binding sites for Ca^{2+} that could change membrane mechanics potentially by altering the interaction between adjacent lipids (Ito and Ohnishi, 1974; Melcrova et al., 2016). The sensitivity of stereocilia membrane diffusivity to extracellular Ca^{2+} appears independent of the MET channel activity as similar results were obtained in both rows. However, low extracellular Ca^{2+} modulates MET channel resting P_o, as well as membrane diffusivity, suggesting a common mode of regulation.

Effect of Voltage on Membrane Diffusivity

Voltage modulates the MET channel P_o in a time-dependent manner in the mammalian OHCs (Peng et al., 2016). Although resting P_o suggests a time independent steady-state measurement reflecting channel open probability when the bundle is not stimulated, with depolarization there is a temporal component where the P_o rapidly increases and then slowly reduces, reflecting a non-steady state condition. We term this P_o^*, simply to indicate the same measurement (a non-externally stimulated hair bundle) but under non-steady-state conditions. GsMTx4 inhibits the voltage modulation suggesting an involvement of the membrane in regulating P_o^*. We investigated the effect of voltage on the stereociliary membrane diffusivity of di-3-ANEPPDHQ during prolonged depolarization to +76 mV. Firstly, we characterized how the P_o^* changes with voltage in mammalian IHCs by stimulating the bundles with large negative and positive sinusoidal displacements delivered with a fluid jet pipette during prolonged depolarization for 22 s (Figure 4A). We also investigated the dependence of voltage modulation of P_o^* on internal Ca^{2+} buffer using 0.1 mM BAPTA or 10 mM BAPTA internally. The MET channel P_o^* rose to a maximum rapidly upon depolarization, followed by a slow decrease to a steady-state value during prolonged depolarization. The timing and extent of the response were sensitive to the internal Ca^{2+} buffer (Figures 4B and 4C). The maximum P_o^* with depolarization to +76 mV was 26.1 ± 10.7% with 0.1 mM BAPTA, which was significantly lower (t test, p < 0.001) than that with 10 mM BAPTA which peaked at 45.1 ± 6.5% (Figure 4D). Also, the time to peak P_o^* was significantly longer for cells with 0.1 mM BAPTA internal compared to 10 mM BAPTA internal, measuring 2.7 ± 1.4 s and 0.38 ± 0.4 s for 0.1 mM BAPTA and 10 mM BAPTA, respectively (Figure 4F).

During prolonged depolarization, P_o^* decreased slowly to a steady state of 18.6 ± 9.2% for 0.1 mM BAPTA which was significantly lower (t test, p < 0.001) than that of 10 mM BAPTA internal measured as 25.4 ± 4.5% (Figure 4D). Also, the change in P_o^* from the peak to the steady state was significantly lower for 0.1 mM BAPTA (7.4 ± 4.9%) compared to 10 mM BAPTA (19.6 ± 4.1%). Thus, the data suggest that the time-dependent voltage modulation of P_o^* is dependent on the internal Ca^{2+} buffering.

We next examined whether voltage affects the stereociliary membrane diffusivity in a time-dependent manner, more specifically during the initial depolarization when we see a rapid increase in the P_o^* and during prolonged depolarization which results in a slow reduction of P_o^* to a steady state. FRAP measurements were done either during the first 12 s of depolarization (early FRAP) to capture changes responsible for the increase in P_o^* or after the first 10 s of depolarization (late FRAP) to capture the reduction of the P_o^* over time, as illustrated in Figures 5A and 5B. Figures 5C and 5D summarize average FRAP curves measured across the two rows of stereocilia comparing early FRAP and late FRAP done at +76 mV to FRAP measured at −84 mV either with 0.1 mM BAPTA or 10 mM BAPTA internal. There was no change in the recovery for early FRAP in any condition while there was a slight increase in the recovery with late FRAP in both stereociliary rows and with both internal buffers. FRAP measurements during the early depolarization resulted in no change in the diffusion constant (Figures 5E and 5G). As FRAP is an average measure across a large volume and an extended time course, it is possible that any localized and fast membrane diffusivity changes due to early depolarization response may not be fully detected in these measurements. The stereociliary membrane diffusion constants were significantly increased in row 2 with late depolarization (paired t test, p < 0.01), from 3.9 ± 0.4 μm^2/s to 4.9 ± 1.1 μm^2/s with 0.1 mM BAPTA internal (Figure 5F) but not for row 1. Diffusivity reduced significantly for both stereociliary rows with 10 mM BAPTA internal, from 3.8 ± 0.9 μm^2/s to 5.1 ± 1.3 μm^2/s for row 1 (paired t test, p < 0.01) and 3.7 ± 0.4 μm^2/s to 4.9 ± 0.7 μm^2/s for row 2 (paired t test, p < 0.05) (Figure 5H).
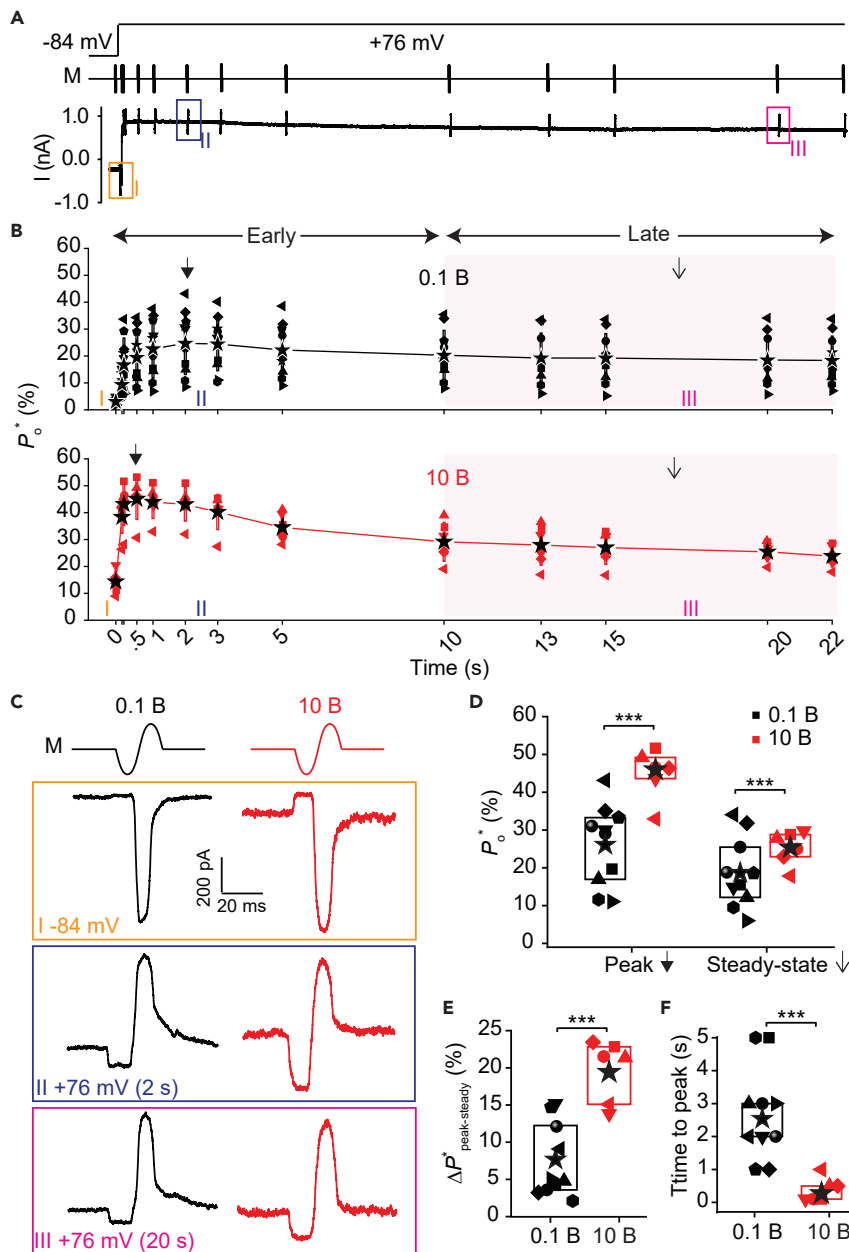
Figure 4. Depolarization Modulates MET P_o*

(A) presents mechanical stimulus (M) and voltage step at the top and a representative current response at the bottom. Depolarization to +76 mV results in an immediate increase in the MET channel P_o*, with P_o* decreasing and stabilizing with prolonged depolarization in IHCs.

(B) Summary plot showing the change in P_o* during depolarization for 22 s for 0.1 mM BAPTA (top) and 10 mM BAPTA (bottom) internal solutions. The values measured at −84 mV are represented at time 0. Each symbol indicates a cell for a given internal solution. The peak P_o* and the steady-state P_o* (average of P_o* values after the time point when change in P_o* is ≤5%) are highlighted with black arrows.

(C) Expanded view of MET current response to a single period of a sinusoidal stimulus (M) from the current plot in (A), highlighted as I, II, and III, for different internal solutions; 0.1 mM BAPTA (black traces) and 10 mM BAPTA (red traces) for −84 mV (top panel), +76 mV at 2 s (middle), and +76 mV at 20 s (bottom).

(D and E) Summary plot of the peak P_o*and steady state P_o* in (D) and ΔP_o* (peak P_o* - steady state P_o*) in (E) showing significant differences between 0.1 mM BAPTA (black symbols) and 10 mM BAPTA (red symbols) internal solutions (t test,

Figure 4. *Continued*

p < 0.001). Each symbol indicates a cell for a given internal solution, with n = 10 cells for 0.1 mM BAPTA and n = 6 cells for 10 mM BAPTA.

(F) Summary plot of the time taken to reach the peak P_o* for different internal solutions. Each symbol indicates a cell for a given internal solution, with n = 10 cells for 0.1 mM BAPTA and n = 6 cells for 10 mM BAPTA.

Boxes represent SDs and the star symbol indicates the mean. 0.1 B, 0.1 mM BAPTA; 10 B, 10 mM BAPTA. ***p < 0.001.

To determine whether the differences observed after prolonged depolarization were unique to stereocilia, we also performed FRAP experiments in IHC soma. Using 10 mM BAPTA, we found no difference in diffusivity due to voltage (Figure S7). Thus, we conclude that voltage-dependent diffusivity changes are unique to the stereociliary membrane.

DISCUSSION

Stereocilia membrane properties were investigated under conditions known to alter MET channel resting P_o to assess more directly the hypothesis that the lipid bilayer modulates the effect of Ca^{2+} and voltage on mammalian auditory MET channels. We show that the IHC stereocilia membrane is highly diffusive compared to the soma, with both stereociliary rows having similar membrane diffusivity. We further demonstrate that the diffusivity of the stereocilia lipid membrane is sensitive to Ca^{2+} and voltage while the basolateral membrane is not. Membrane diffusivity is not modulated by MET; however, the strong correlation between the resting P_o and diffusivity suggests that membrane mechanics and MET channel resting P_o have a common underlying modulator (Figure 6A).

High Membrane Diffusivity of the IHC Stereocilia

IHC stereocilia showed significantly higher diffusion constants (∼9 times) than the soma, consistent with reported elevated diffusion constants for guinea pig OHC stereocilia bundles compared to the soma (Boutet de Monvel et al., 2006). Diffusion constants measured for di-3-ANEPPDHQ in the IHC soma ranged from 0.4 to 0.7 μm^2/sec, comparable to the previously reported values for di-8-ANEPPS in IHCs and OHCs ranging 0.2–1 μm^2/sec (Oghalai et al., 2000, Boutet De Monvel et al., 2006; Chen and Zhao, 2007; Organ and Raphael, 2009). All measured values are within the range typically reported for living cells, i.e., 0.01–10 μm^2/sec with most cells exhibiting values from 0.1 to 1 μm^2/sec at 18–22°C (Lee and Jacobson, 1994; Almeida and Vaz, 1995). However, the IHC stereocilia values are significantly higher than soma values at 20–22°C using the same lipid dye; similar high values at room temperature are observed in a few cell types such as rat smooth muscle cells and mouse spleen and lymphocytes (Lee and Jacobson, 1994). Membrane diffusivity differences may arise from different lipid composition, protein content, membrane interaction with underlying cytoskeletal structures, mechanotransduction machinery, active lipid transport, and/or membrane curvature (Hoekstra, 1994; Bigay and Antonny, 2012).

Lipid Composition

Mass spectrometry of chick vestibular hair bundles suggests that the stereocilia lipid composition does not differ significantly from other cell membranes, except for higher level of sphingomyelin and ceramide (Zhao et al., 2012). Therefore, it is less likely that the high stereociliary diffusivity is due to gross differences in lipid composition. However, compartmentalization of specific lipids or even low levels of some lipids can have dramatic effects on membrane mechanics; therefore, we cannot completely exclude lipid composition as a contributor.

Protein Content and Cytoskeleton

The presence of distinct transmembrane proteins, sub-membranous scaffolding proteins, and proteins that link the membrane to the underlying dense actin cytoskeleton would support the stereocilia membrane being less diffusive (Owen, 2015) and so are unlikely responsible for the elevated stereocilia diffusivity. It is possible, though unlikely, that all cell membranes have high levels of proteins embedded and have strong cytoskeletal connections leading to low diffusivity, and it is the lack of proteins and cytoskeletal interactions contributing to the higher stereociliary diffusivity levels.

Mechanotransduction Machinery

MET channels are only present in the shorter stereocilia rows (Beurg et al., 2009). The upper tip-link insertion point has a density with selective molecules like harmonin, whirlin, and cadherin 23, while the lower insertion point is linked via protocadherin 15, CIB2 (Calcium And Integrin Binding Family Member 2),
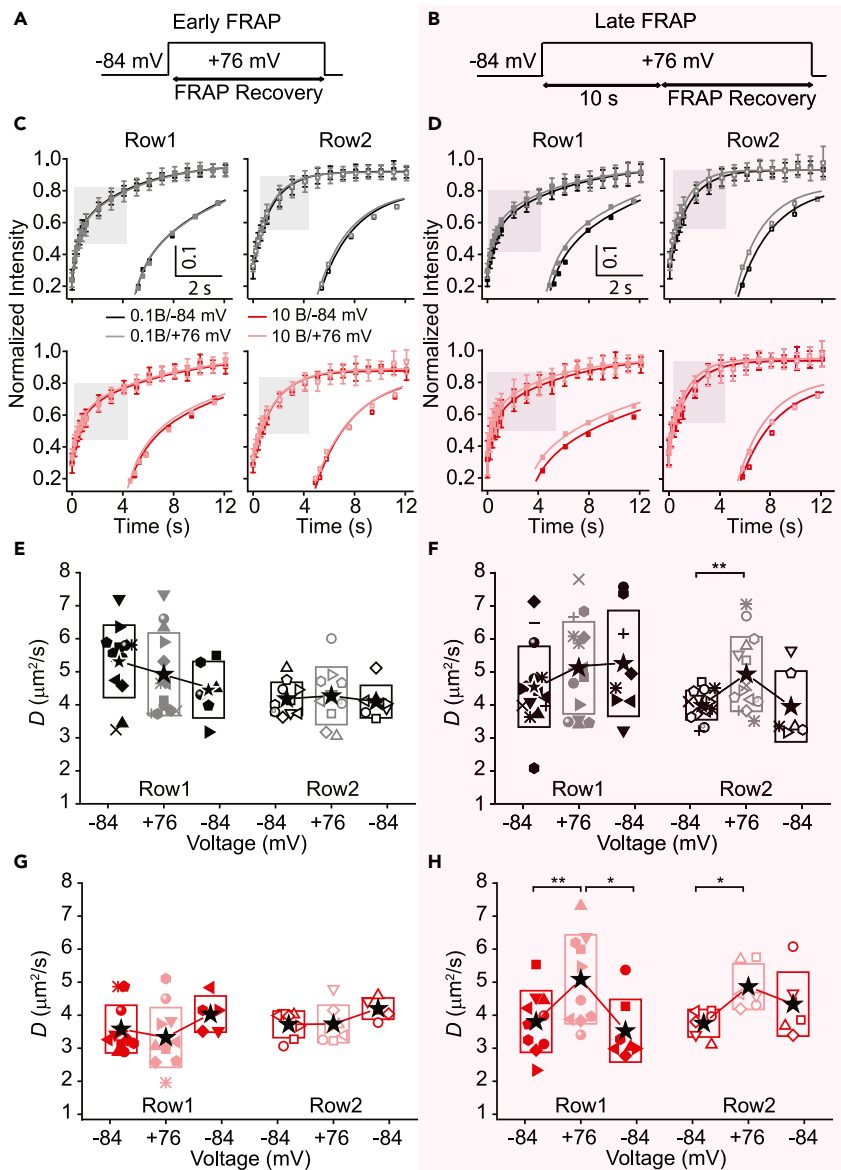
Figure 5. Prolonged Depolarization Increases Stereociliary Membrane Diffusivity

(A and B) Illustration of the FRAP timing with respect to depolarization showing (A) early FRAP, where FRAP recovery phase starts at time 0 of depolarization, and (B) late FRAP, where FRAP recovery phase starts 10 s after depolarization.

(C) Average early FRAP curves (mean ± SD) measured from row 1 (left side) and row 2 (right side) stereocilia, with 0.1 mM (top) and 10 mM BAPTA (bottom) internal solutions, showing no difference between the measurements at −84 mV (black and red traces) and +76 mV (gray and light red traces).

(D) Average late FRAP curves (mean ± SD) show faster recovery with prolonged depolarization to +76 mV (gray and light red traces) compared to that of −84 mV (black and red traces).

(E) and (G) Summary of cells with 0.1 mM BAPTA (E) and 10 mM BAPTA (G) internal solutions showing that early depolarization from -84 mV (black symbols in E and red symbols in G) to +76 mV (grey symbols in E and and light red symbols in G) has no significant effect on the diffusion constants in both stereocilia rows as well as with 0.1 and 10 mM BAPTA internal solutions. Each colored/patterned symbol corresponds to a bundle/cell.

(F) and (H) Summary plot of D values with 0.1 mM BAPTA (F) and 10 mM BAPTA (H) internal solutions showing that late depolarization significantly increases the diffusion constant of row 2 irrespective of the internal solution and of the row 1 with 10 mM BAPTA (paired t test, $p < 0.05$). Each colored/patterned symbol corresponds to a bundle/cell.

Boxes represent SDs, and the star symbol indicate the mean. 0.1 B, 0.1 mM BAPTA; 10 B, 10 mM BAPTA. $*p < 0.05$, $**p < 0.01$, $***p < 0.001$.
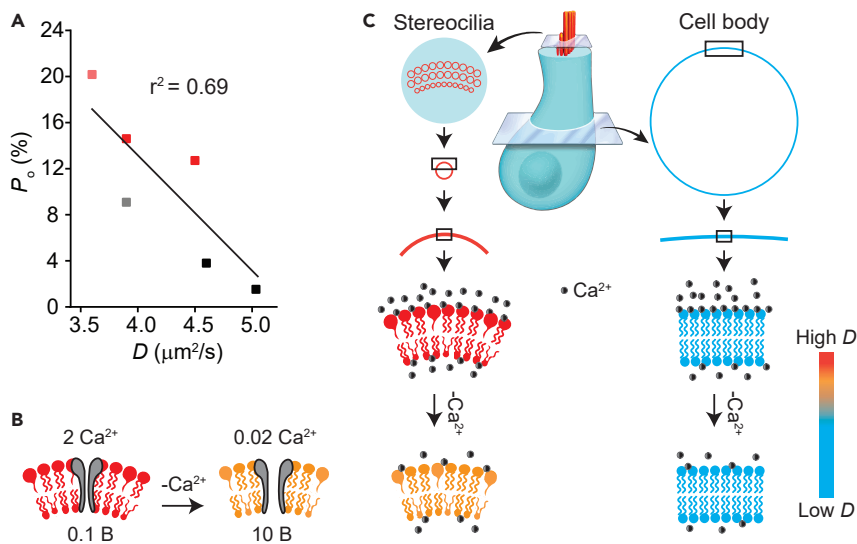
Figure 6. MET Resting P_o Is Correlated to Stereociliary Membrane Diffusivity

(A) The mean MET resting P_o plotted against the mean diffusion constant D measured across experiments shows a strong correlation ($r^2 = 0.69$, $p < 0.05$), with black symbols representing measurements taken with 0.1 mM BAPTA internal solution/2 mM external Ca^{2+} at −80 mV holding potential, red symbols representing 10 mM BAPTA internal solution/2 mM external Ca^{2+} at −80 mV holding potential, gray symbols representing 0.1 mM BAPTA internal solution/20 μM external Ca^{2+} at −80 mV holding potential, and salmon symbols representing 10 mM BAPTA.

(B) presents the relationship in (A) pictorially, suggesting that the MET P_o is sensitive to membrane diffusivity. The stereocilia membrane curvature presented is not scaled as the exact curvature value would depend on the exact position of the MET channel on the stereocilia, which is unknown.

(C) Schematic illustrating the difference in membrane curvature between the stereocilia wrapping around its actin core and the basolateral membrane. The white cross sections on the hair bundle and the cell body indicate the approximate location of the represented membrane curvatures for the stereocilia (in red) and basolateral membrane (in blue). The cartoon denotes the need for specialized conical lipids on the outer and inner leaflets to accommodate for the observed curvature. The cartoon is not a scaled representation of the relation between lipid bilayer thickness and curvature as that would make it impossible to see the individual lipids. The lipids are colored to indicate the range of diffusivity with red representing high diffusivity and blue representing low diffusivity. We hypothesize that the inherent curvature alters the sensitivity of the stereocilia to divalent ions which alters diffusivity and can indirectly alter MET channel P_o.

LHFPL5 (Lipoma HMGIC fusion partner-like 5), TMIE (Transmembrane Inner Ear), and TMC (Transmembrane channel-like) molecules (Kazmierczak et al., 2007; Xiong et al., 2012; Kurima et al., 2015; Giese et al., 2017; Pan et al., 2018; Cunningham et al., 2020; Krey et al., 2020). The MET channel at the lower end of the tip links permeates calcium and monovalent ions into this small volume. Yet, our data show that both stereociliary rows have similar baseline membrane diffusivity and similar changes in diffusivity following Ca^{2+} and voltage manipulations, indicating that the observed effects are independent of MET channel activity. Additionally, pharmacologically blocking MET channels had no effect on diffusivity, suggesting that the MET channel complex does not regulate macroscopic membrane diffusivity. Thus, it is unlikely the mechanotransduction machinery is responsible for the differences between soma and stereocilia.

Active Transport

High stereociliary diffusivity could also arise from an active lipid transport component coupled with passive diffusion. The stereociliary membrane specifically expresses phospholipid-translocating ATPases such as ATP8B1, which are essential in phospholipid transport to maintain membrane asymmetry and curvature (Sebastian et al., 2012; Coleman et al., 2013), and morphological and functional degeneration of the hair bundles due to the deficiency of ATP8B1 and ATP8A2 indicate the importance of this transport mechanism involved in maintaining the lipid composition and the mechanical stability of the stereocilia (Stapelbroek et al., 2009; Coleman et al., 2014). The functional relevance of this active lipid transport is unclear. Whether this transport can account for the large difference in diffusivity is also unclear, and further experiments are needed to address this possibility.

Membrane Curvature

A simple yet plausible mechanism for elevated stereociliary diffusivity stems from the mechanics associated with high stereociliary membrane curvature. Membrane curvature is generated by the membrane monolayer asymmetry due to the presence of specific lipids such as conical lipids and clustering of shaped transmembrane proteins (McMahon and Gallop, 2005; Jarsch et al., 2016) required for establishing the tight wrapping of the actin core (Figure 6C). In its simplest form, lipid asymmetry is required for the membrane to ensheath the actin core of the stereocilia. Importantly, membrane curvature can mechanically control the spatial organization of the lipid bilayer, with regions of high curvature leading to loose lipid packing (i.e., high diffusivity) due to the preferential localization of disordered lipid domains (Parthasarathy et al., 2006; Bigay and Antonny, 2012; Vamparys et al., 2013). Parthasarathy et al. found a critical curvature of <0.8 μm^2, where spatial organization of lipids are directly affected by curvature (Parthasarathy et al., 2006). Thus, membranes of IHC stereocilia having curvatures greater than 1 μm^2 can be mechanically stressed and thus likely impacting membrane diffusivity by the spatial organization of lipid domains, as seen in other membrane protrusions such as filopodia and microvilli (Zhao et al., 2013; Prévost et al., 2015). The observed similar high stereociliary membrane diffusivity in both rows of stereocilia (with similar diameters) may in part be established by the curvature associated with the dimensions of the stereocilia.

FRAP is a slow measurement that averages across a large membrane volume. Stereocilia membranes are described with bumps potentially representing transmembrane proteins. It is also likely that the membrane is not longitudinally uniform, with MET machinery at the tops of the shorter rows and with the tip membrane undergoing deformation via the tip link pulling (either directly or indirectly). FRAP is not reporting on nanodomain differences in diffusivity; alternate technologies are needed for this level of resolution.

How Might the Stereociliary Membrane Be Affected Differently from the Soma?

Data demonstrate Ca^{2+} and voltage effects on stereociliary membrane diffusivity but not on the basolateral membrane. Multivalent ions, especially Ca^{2+}, can directly interact with lipids to change the membrane mechanical properties (Ito and Ohnishi, 1974; Shoemaker and Vanderlick, 2003; Melcrova et al., 2016). Ca^{2+} can change lipid packing or membrane order through conformational changes to lipid headgroups, ordering of acyl chains, affecting the hydration shell of lipid headgroups, and altering the repulsive interactions between the lipids. The baseline diffusivity associated with the bilayer wrapping around the stereocilia may simply reflect the above changes better than the soma such that a 10% change is easily detectable in the stereocilia ($\sim$0.5 μm^2/s) but less so in the soma (0.05 μm^2/s). Alternatively, the curvature tension of the stereocilia may create an environment more sensitive to divalent modulation (Figure 6C).

The effects of voltage on stereocilia diffusivity are similarly complex as the effects on MET P_o. The differential effect on stereocilia as compared to soma may be as described above, a reflection of membrane curvature impacting lipid distributions. The lack of effect on diffusivity during the initial depolarization where P_o is increasing is likely due to the slow temporal resolution of FRAP, and better technology is needed to characterize fast responses. The slower increase in diffusivity correlates with a reduction in P_o and suggests a reduction in force transference to the channel. The underlying molecular mechanism for this effect and the physiological relevance remain to be elucidated. The simplest explanation may be a rearrangement of lipid molecules due to charged headgroups being less shielded by calcium ions.

Implications for Hair Cell Mechanotransduction

The nine-fold difference in membrane diffusivity between the stereocilia and soma is likely to provide the necessary lipid environment for modulation of mechanotransduction, the key functional output of this organelle. High membrane diffusivity is often associated with elevated membrane tension and reduced hydrophobic thickness (Butler et al., 2001; Haidekker et al., 2001; Blood et al., 2005; Reddy et al., 2012). Studies of other mechanosensitive channels show that decreased membrane fluidity increases their activation threshold, and thinner membrane favors channel opening (Perozo et al., 2002; Nomura et al., 2012). In contrast, stereociliary membrane diffusivity is generally high while the MET resting P_o is low, and the P_o increases as diffusivity is reduced (Figures 6A and 6B), at least in the range of measured diffusivity. The opposite polarity for hair cell MET channel sensitivity may be simply due to how force is transmitted to the MET channel. While many mechanosensitive channels sense force transmitted directly through the membrane, hair cell channels are thought to be tethered to both an extracellular and intracellular link (Effertz et al., 2015). Thus, the mechanical contribution of the bilayer may be indirect or in parallel to the protein coupling which in its simplest form would reverse sensitivity. More work is needed to clarify this important point.

Our data support a potential mechanism whereby the stereociliary membrane has a significantly higher baseline membrane diffusivity compared to the soma likely due to the high curvature of the stereociliary membrane. The differential Ca^{2+} effect on the stereociliary membrane may also be a manifestation of curvature-induced stress, where the stereocilia and the soma are at different curvature tension such that Ca^{2+} differentially affects lipid packing and thus the membrane diffusivity of these structures. MET channels do not contribute to stereociliary diffusivity but may be directly or indirectly modulated by changes in diffusivity as indicated by the resting open probability. We postulate that the stereociliary membrane contributes to a viscoelastic-like component modulating the hair cell MET channel.

Limitations of the Study

FRAP measurements are both spatially and temporally limited given that recovery times are a function of the volume bleached and the ability to image at high rates. The technology does not allow for monitoring rapid changes in membrane properties. Additionally, the volume is typically dictated by the z-resolution of the objective (as set by the numerical aperture of the objective) and so local changes will be filtered or averaged into the larger volume being monitored. Thus, the technology is unlikely to detect changes associated with MET channel gating, for example, because gating is both very local and fast. An example is that FRAP does not detect a change during the rapid change in MET open probability with depolarization. These data cannot be interpreted as there is no membrane effect but simply that FRAP does not detect a change. Related to the spatial and temporal limitations is the fact that the relationship between MET open probability and membrane diffusivity is a correlation; additional technologies are needed to generate causal links between open probability and membrane mechanics. Data presented here provide the impetus to follow-up on developing technologies to investigate causality.

Resource Availability

Lead Contact

Further information and requests for resources should be directed to and will be fulfilled by the lead contact, Prof. Anthony Ricci, aricci@stanford.edu.

Materials Availability

This study did not generate new unique reagents.

Data and Code Availability

The original unprocessed data of live cell imaging and electrophysiological recordings are contained in very large files. These are available upon request from the corresponding author. All codes have been uploaded to Mendeley Data "Mendeley Data:https://doi.org/10.17632/3wrd9xp4gc.1." and are also available through the authors.

METHODS

All methods can be found in the accompanying Transparent Methods supplemental file.

SUPPLEMENTAL INFORMATION

Supplemental Information can be found online at https://doi.org/10.1016/j.isci.2020.101773.

AUTHOR CONTRIBUTIONS

S.S.G. and A.J.R. designed the experiments; S.S.G. performed the experiments; C.R.S. developed and implemented the diffusion model for stereocilia and soma; S.S.G. and A.J.R. analyzed the data, interpreted the results, and wrote the manuscript.

DECLARATION OF INTERESTS

The authors declare no competing interests.

REFERENCES

Almeida, P.F.F., and Vaz, W.L. (1995). Lateral Diffusion in Membranes. Handbook of Biological Physics (Elsevier Science).

Ayee, M.A., and Levitan, I. (2016). Paradoxical impact of cholesterol on lipid packing and cell stiffness. Front. Biosci. Landmark 21, 1245–1259.

Bagatolli, L.A. (2006). To see or not to see: lateral organization of biological membranes and fluorescence microscopy. Biochim. Biophys. Acta 1758, 1541–1556.

Beurg, M., Fettiplace, R., Nam, J.H., and Ricci, A.J. (2009). Localization of inner hair cell mechanotransducer channels using high-speed calcium imaging. Nat. Neurosci. 12, 553–558.

Bigay, J., and Antonny, B. (2012). Curvature, lipid packing, and electrostatics of membrane organelles: defining cellular territories in determining specificity. Dev. Cell 23, 886–895.

Blood, P.D., Ayton, G.S., and Voth, G.A. (2005). Probing the molecular-scale lipid bilayer response to shear flow using nonequilibrium molecular dynamics. J. Phys. Chem. B 109, 18673–18679.

Boutet de Monvel, J., Brownell, W.E., and Ulfendahl, M. (2006). Lateral diffusion anisotropy and membrane lipid/skeleton interaction in outer hair cells. Biophysical J. 91, 364–381.

Bowman, C.L., Gottlieb, P.A., Suchyna, T.M., Murphy, Y.K., and Sachs, F. (2007). Mechanosensitive ion channels and the peptide inhibitor GsMTx-4: history, properties, mechanisms and pharmacology. Toxicon 49, 249–270.

Butler, P.J., Norwich, G., Weinbaum, S., and Chien, S. (2001). Shear stress induces a time-and position-dependent increase in endothelial cell membrane fluidity. Am. J. Physiol 280, C962–C969.

Chen, G.D., and Zhao, H.B. (2007). Effects of intense noise exposure on the outer hair cell plasma membrane fluidity. Hearing Res. 226, 14–21.

Coleman, J.A., Quazi, F., and Molday, R.S. (2013). Mammalian P4-ATPases and ABC transporters and their role in phospholipid transport. Biochim. Biophys. Acta 1831, 555–574.

Coleman, J.A., Zhu, X., Djajadi, H.R., Molday, L.L., Smith, R.S., Libby, R.T., John, S.W., and Molday, R.S. (2014). Phospholipid flippase ATP8A2 is required for normal visual and auditory function and photoreceptor and spiral ganglion cell survival. J. Cell Sci. 127, 1138–1149.

Crawford, A.C., Evans, M.G., and Fettiplace, R. (1991). The actions of calcium on the mechano-electrical transducer current of turtle hair cells. J. Physiol. 434, 369–398.

Cunningham, C.L., Qiu, X., Wu, Z., Zhao, B., Peng, G., Kim, Y.H., Lauer, A., and Muller, U. (2020). TMIE defines pore and gating properties of the mechanotransduction channel of mammalian cochlear hair cells. Neuron 107, 126–143 e128.

Effertz, T., Becker, L., Peng, A.W., and Ricci, A.J. (2017). Phosphoinositol-4,5-Bisphosphate regulates auditory hair-cell mechanotransduction-channel pore properties and fast adaptation. J. Neurosci. 37, 11632–11646.

Effertz, T., Scharr, A.L., and Ricci, A.J. (2015). The how and why of identifying the hair cell mechano-electrical transduction channel. Pflügers Archiv 467, 73–84.

Farris, H.E., LeBlanc, C.L., Goswami, J., and Ricci, A.J. (2004). Probing the pore of the auditory hair cell mechanotransducer channel in turtle. J. Physiol. 558, 769–792.

Fettiplace, R. (1992). The role of calcium in hair cell transduction. Sensory Transduction 47, 344–356.

Gianoli, F., Risler, T., and Kozlov, A.S. (2017). Lipid bilayer mediates ion-channel cooperativity in a model of hair-cell mechanotransduction. Proc. Natl. Acad. Sci. U S A 114, E11010–E11019.

Giese, A.P., Tang, Y.-Q., Sinha, G.P., Bowl, M.R., Goldring, A.C., Parker, A., Freeman, M.J., Brown, S.D., Riazuddin, S., and Fettiplace, R. (2017). CIB2 interacts with TMC1 and TMC2 and is essential for mechanotransduction in auditory hair cells. Nat. Commun. 8, 1–13.

Gillespie, P.G., and Müller, U. (2009). Mechanotransduction by hair cells: models, molecules, and mechanisms. Cell 139, 33–44.

Glowatzki, E., Ruppersberg, J.P., Zenner, H.P., and Rusch, A. (1997). Mechanically and ATP-induced currents of mouse outer hair cells are independent and differentially blocked by d-tubocurarine. Neuropharmacology 36, 1269–1275.

Haidekker, M.A., Ling, T., Anglo, M., Stevens, H.Y., Frangos, J.A., and Theodorakis, E.A. (2001). New fluorescent probes for the measurement of cell membrane viscosity. Chem. Biol. 8, 123–131.

Hirono, M., Denis, C.S., Richardson, G.P., and Gillespie, P.G. (2004). Hair cells require phosphatidylinositol 4, 5-bisphosphate for mechanical transduction and adaptation. Neuron 44, 309–320.

Hoekstra, D. (1994). Cell Lipids (Academic Press).

Ito, T., and Ohnishi, S.I. (1974). Ca2+-Induced lateral phase separations in phosphatic acid-phosphatidylcholine membranes. Biochim. Biophys. Acta 352, 29–37.

Jarsch, I.K., Daste, F., and Gallop, J.L. (2016). Membrane curvature in cell biology: an integration of molecular mechanisms. J. Cell Biol. 214, 375–387.

Kazmierczak, P., Sakaguchi, H., Tokita, J., Wilson-Kubalek, E.M., Milligan, R.A., Müller, U., and Kachar, B. (2007). Cadherin 23 and protocadherin 15 interact to form tip-link filaments in sensory hair cells. Nature 449, 87–91.

Kirkwood, N.K., O'Reilly, M., Derudas, M., Kenyon, E.J., Huckvale, R., van Netten, S.M., Ward, S.E., Richardson, G.P., and Kros, C.J. (2017). D-Tubocurarine and berbamine: alkaloids that are permeant blockers of the hair cell's mechano-electrical transducer channel and protect from aminoglycoside toxicity. Front. Cell Neurosci. 11, 262.

Krey, J.F., Chatterjee, P., Dumont, R.A., O'Sullivan, M., Choi, D., Bird, J.E., and Barr-Gillespie, P.G. (2020). Mechanotransduction-dependent control of stereocilia dimensions and row identity in inner hair cells. Curr. Biol. 30, 442–454.e7.

Kurima, K., Ebrahim, S., Pan, B., Sedlacek, M., Sengupta, P., Millis, B.A., Cui, R., Nakanishi, H., Fujikawa, T., and Kawashima, Y. (2015). TMC1 and TMC2 localize at the site of mechanotransduction in mammalian inner ear hair cell stereocilia. Cell Rep. 12, 1606–1617.

Lee, G.M., and Jacobson, K. (1994). Lateral mobility of lipids in membranes. In Cell Lipids: Current Topics in Membranes, D. Hoekstra, ed. (Academin Press, Inc), pp. 111–143.

Martinac, B., and Poole, K. (2018). Mechanically activated ion channels. Int. J. Biochem. Cell Biol. 97, 104–107.

McMahon, H.T., and Gallop, J.L. (2005). Membrane curvature and mechanisms of dynamic cell membrane remodelling. Nature 438, 590–596.

Melcrova, A., Pokorna, S., Pullanchery, S., Kohagen, M., Jurkiewicz, P., Hof, M., Jungwirth, P., Cremer, P.S., and Cwiklik, L. (2016). The complex nature of calcium cation interactions with phospholipid bilayers. Sci. Rep. 6, 38035.

Nguyen, T.V.N., and Brownell, W.E. (1998). Contribution of membrane cholesterol to outer hair cell lateral wall stiffness. Otolaryngol.Head Neck Surg. 119, 14–20.

Nomura, T., Cranfield, C.G., Deplazes, E., Owen, D.M., Macmillan, A., Battle, A.R., Constantine, M., Sokabe, M., and Martinac, B. (2012). Differential effects of lipids and lyso-lipids on the mechanosensitivity of the mechanosensitive channels MscL and MscS. Proc. Natl. Acad. Sci. U S A *109*, 8770–8775.

Oghalai, J.S., Zhao, H.B., Kutz, J.W., and Brownell, W.E. (2000). Voltage- and tension-dependent lipid mobility in the outer hair cell plasma membrane. Science *287*, 658–661.

Organ, L.E., and Raphael, R.M. (2009). Lipid lateral mobility in cochlear outer hair cells: regional differences and regulation by cholesterol. J. Assoc. Res. Otolaryngol. *10*, 383–396.

Owen, D.M. (2015). Methods in Membrane Lipids (Humana Press).

Pan, B., Akyuz, N., Liu, X.-P., Asai, Y., Nist-Lund, C., Kurima, K., Derfler, B.H., György, B., Limapichat, W., and Walujkar, S. (2018). TMC1 forms the pore of mechanosensory transduction channels in vertebrate inner ear hair cells. Neuron *99*, 736–753.e736.

Parasassi, T., Gratton, E., Yu, W.M., Wilson, P., and Levi, M. (1997). Two-photon fluorescence microscopy of Laurdan generalized polarization domains in model and natural membranes. Biophysical J. *72*, 2413–2429.

Parthasarathy, R., Yu, C.-H., and Groves, J.T. (2006). Curvature-modulated phase separation in lipid bilayer membranes. Langmuir *22*, 5095–5099.

Peng, A.W., Effertz, T., and Ricci, A.J. (2013). Adaptation of mammalian auditory hair cell mechanotransduction is independent of calcium entry. Neuron *80*, 960–972.

Peng, A.W., Gnanasambandam, R., Sachs, F., and Ricci, A.J. (2016). Adaptation independent modulation of auditory hair cell mechanotransduction channel open probability implicates a role for the lipid bilayer. J. Neurosci. *36*, 2945–2956.

Peng, A.W., Salles, F.T., Pan, B.F., and Ricci, A.J. (2011). Integrating the biophysical and molecular mechanisms of auditory hair cell mechanotransduction. Nat. Commun. *2*, 523.

Perozo, E., Kloda, A., Cortes, D.M., and Martinac, B. (2002). Physical principles underlying the transduction of bilayer deformation forces during mechanosensitive channel gating. Nat. Struct. Biol. *9*, 696–703.

Pickles, J.O., Comis, S.D., and Osborne, M.P. (1984). Cross-links between stereocilia in the Guinea-pig organ of corti, and their possible relation to sensory transduction. Hearing Res. *15*, 103–112.

Powers, R.J., Kulason, S., Atilgan, E., Brownell, W.E., Sun, S.X., Barr-Gillespie, P.G., and Spector, A.A. (2014). The local forces acting on the mechanotransduction channel in hair cell stereocilia. Biophysical J. *106*, 2519–2528.

Powers, R.J., Roy, S., Atilgan, E., Brownell, W.E., Sun, S.X., Gillespie, P.G., and Spector, A.A. (2012). Stereocilia membrane deformation: implications for the gating spring and mechanotransduction channel. Biophysical J. *102*, 201–210.

Prévost, C., Zhao, H., Manzi, J., Lemichez, E., Lappalainen, P., Callan-Jones, A., and Bassereau, P. (2015). IRSp53 senses negative membrane curvature and phase separates along membrane tubules. Nat. Commun. *6*, 1–11.

Reddy, A.S., Warshaviak, D.T., and Chachisvilis, M. (2012). Effect of membrane tension on the physical properties of DOPC lipid bilayer membrane. Biochim. Biophys. Acta *1818*, 2271–2281.

Ricci, A.J., and Fettiplace, R. (1997). The effects of calcium buffering and cyclic AMP on mechanoelectrical transduction in turtle auditory hair cells. J. Physiol. *501*, 111–124.

Ricci, A.J., and Fettiplace, R. (1998). Calcium permeation of the turtle hair cell mechanotransducer channel and its relation to the composition of endolymph. J. Physiol. *506*, 159–173.

Sebastian, T.T., Baldridge, R.D., Xu, P., and Graham, T.R. (2012). Phospholipid flippases: building asymmetric membranes and transport vesicles. Biochim. Biophys. Acta *1821*, 1068–1077.

Shoemaker, S.D., and Vanderlick, T.K. (2003). Calcium modulates the mechanical properties of anionic phospholipid membranes. J. Colloid Interfaces Sci. *266*, 314–321.

Stapelbroek, J.M., Peters, T.A., van Beurden, D.H., Curfs, J.H., Joosten, A., Beynon, A.J., van Leeuwen, B.M., van der Velden, L.M., Bull, L., and Elferink, R.P.O. (2009). ATP8B1 is essential for maintaining normal hearing. Proc. Natl. Acad. Sci. U S A *106*, 9709–9714.

Suchyna, T.M., Johnson, J.H., Hamer, K., Leykam, J.F., Gage, D.A., Clemo, H.F., Baumgarten, C.M., and Sachs, F. (2000). Identification of a peptide toxin from Grammostola spatulata spider venom that blocks cation-selective stretch-activated channels. J. Gen. Physiol. *115*, 583–598.

Tillman, T.S., and Cascio, M. (2003). Effects of membrane lipids on ion channel structure and function. Cell Biochem. Biophys. *38*, 161–190.

Ursell, T., and Blount, P. (2008). Mechanosensitive Ion Channels (Springer).

Vamparys, L., Gautier, R., Vanni, S., Bennett, W.D., Tieleman, D.P., Antonny, B., Etchebest, C., and Fuchs, P.F. (2013). Conical lipids in flat bilayers induce packing defects similar to that induced by positive curvature. Biophysical J. *104*, 585–593.

Xiong, W., Grillet, N., Elledge, H.M., Wagner, T.F., Zhao, B., Johnson, K.R., Kazmierczak, P., and Müller, U. (2012). TMHS is an integral component of the mechanotransduction machinery of cochlear hair cells. Cell *151*, 1283–1295.

Zhao, H., Williams, D.E., Shin, J.-B., Brügger, B., and Gillespie, P.G. (2012). Large membrane domains in hair bundles specify spatially constricted radixin activation. J. Neurosci. *32*, 4600–4609.

Zhao, Y., Liu, J., Yang, C., Capraro, B.R., Baumgart, T., Bradley, R.P., Ramakrishnan, N., Xu, X., Radhakrishnan, R., and Svitkina, T. (2013). Exo70 generates membrane curvature for morphogenesis and cell migration. Dev. Cell *26*, 266–278.
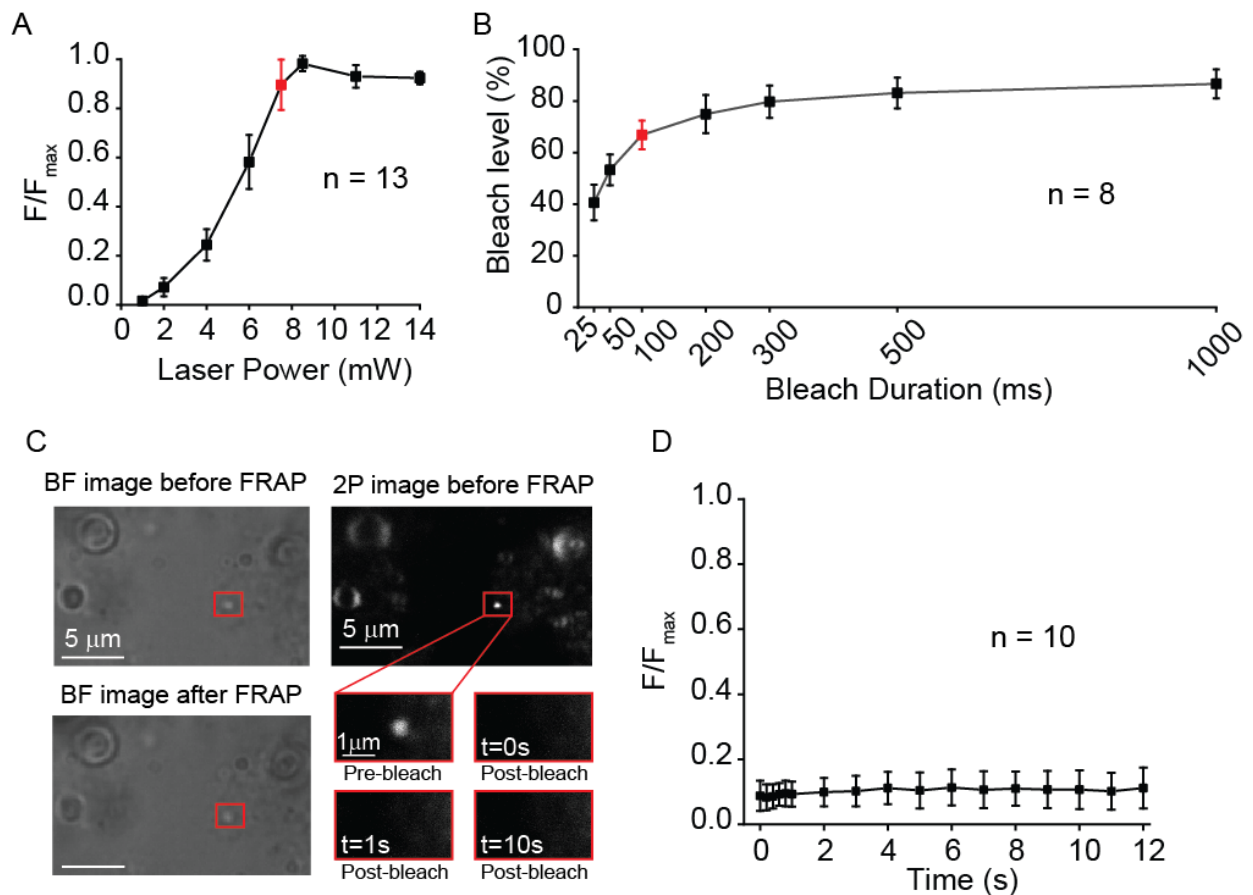
Supplemental Information

Rat Auditory Inner Hair Cell Mechanotransduction

and Stereociliary Membrane Diffusivity

Are Similarly Modulated by Calcium

Shefin S. George, Charles R. Steele, and Anthony J. Ricci

1 **Supplemental Information**

2

A

B

C

BF image before FRAP

2P image before FRAP

5 μm

5 μm

BF image after FRAP

1μm
Pre-bleach

t=0s
Post-bleach

t=1s
Post-bleach

t=10s
Post-bleach

D

3

Figure S1. Characterization of FRAP parameters. Related to Figure 1. (A) Power dependence of the normalized average fluorescence intensity for di-3-ANEPPDHQ excited at 860 nm. The laser power which marks the apparent onset of excitation saturation is highlighted in red. The bleaching power of 7 mW was selected to avoid excitation saturation. (B) Dependence of bleach level on the bleach duration. For this study, bleach duration of 100 ms resulted in ~70% bleaching. (C) Sequence of FRAP images (*right*) illustrating irreversible bleaching of di-3-ANEPPDHQ following complete photobleaching of pure DOPC vesicles. The bright field (BF) images of the bleached vesicle before and after FRAP is shown on the left. (D) Summary of FRAP curves from vesicles (n = 10) shows no recovery in the fluorescence signal after photobleaching, confirming irreversible bleaching of di-3-ANEPPDHQ for the duration of 12 sec. Each data point in (A), (B) and (D) is the mean ± SD.
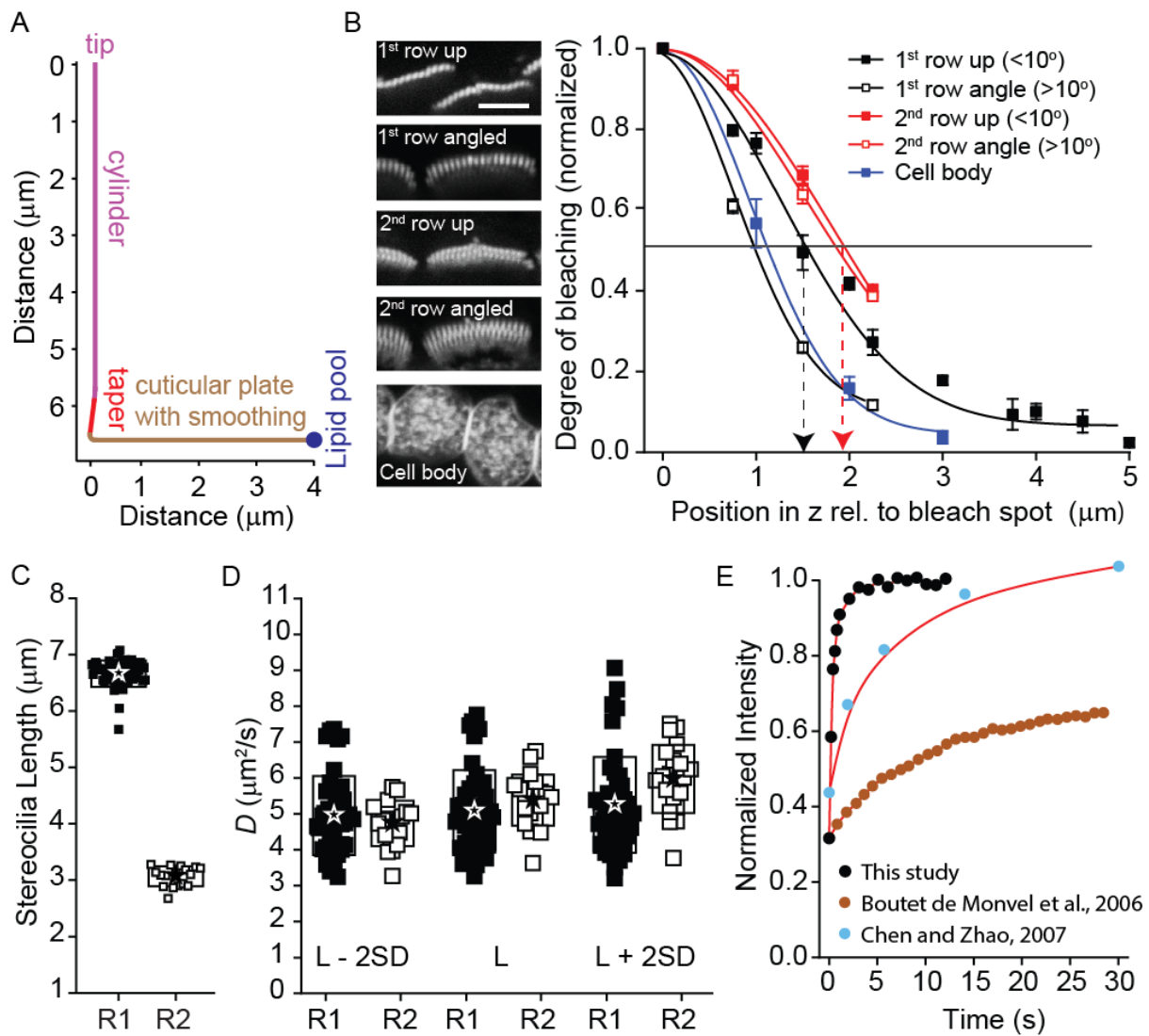
Figure S2. Diffusion model and parameters. Related to Figure 1. (A) One-dimensional diffusion model for cylindrical stereocilia. The schematic uses the length for row1 stereocilia. The lipid pool is assumed to be at 4 μm from the taper on the cuticular plate. (B) Degree of bleaching normalized to its maximum (mean ± SD) measured at different positions along a stereocilium's or cell body's z-axis. Stereociliary rows were either vertical or at an angle of >10°. The black and red dotted arrows indicate the axial bleach extension values used for row1 and row2 stereocilia respectively in our diffusion model. (C) Length measured for stereocilia rows from live P9 rat organ of Corti stained with di-3-ANEPPDHQ. (D) Summary plot illustrating the dependency of the diffusion constant D on the length L of the stereocilia rows. Boxes represent the SDs and the star symbols indicate the means. Each data point is a stereocilium. R1 = row1, R2 = row2. (E) Sample recovery curves from the cell body comparing our data from IHC to previous data obtained from isolated OHCs (Boutet De Monvel et al., 2006, Chen and Zhao, 2007). By accounting for the experimental

30 differences using accurate diffusion model, we extracted similar average diffusion

31 constants of 0.58 µm^2/s compared to 0.3 - 0.46 µm^2/s reported by (Boutet De Monvel et

32 al., 2006) and 0.13 - 0.2 µm^2/s reported by (Chen and Zhao, 2007), even though the time

33 constants are very different between studies.

34

35

	Diffusivity D (µm^2/s)				
	Monvel, et al. (2006)	Chen & Zhao (2007)	Organ and Raphael (2009)	Oghalai et al. (2000)	Present
IHC lateral wall	0.46				0.58
OHC lateral wall	0.30	0.13 - 0.2	1.67	0.13 - 0.7	
Cuticular plate			5.26		
OHC stereocilia	0.7 - 1.1				
IHC stereocilia					5

36
37 **Table S1:** Related to Figure 1. The table lists the mean diffusivity D measured for

38 various cellular membranes of organ of Corti by several studies.

39

40
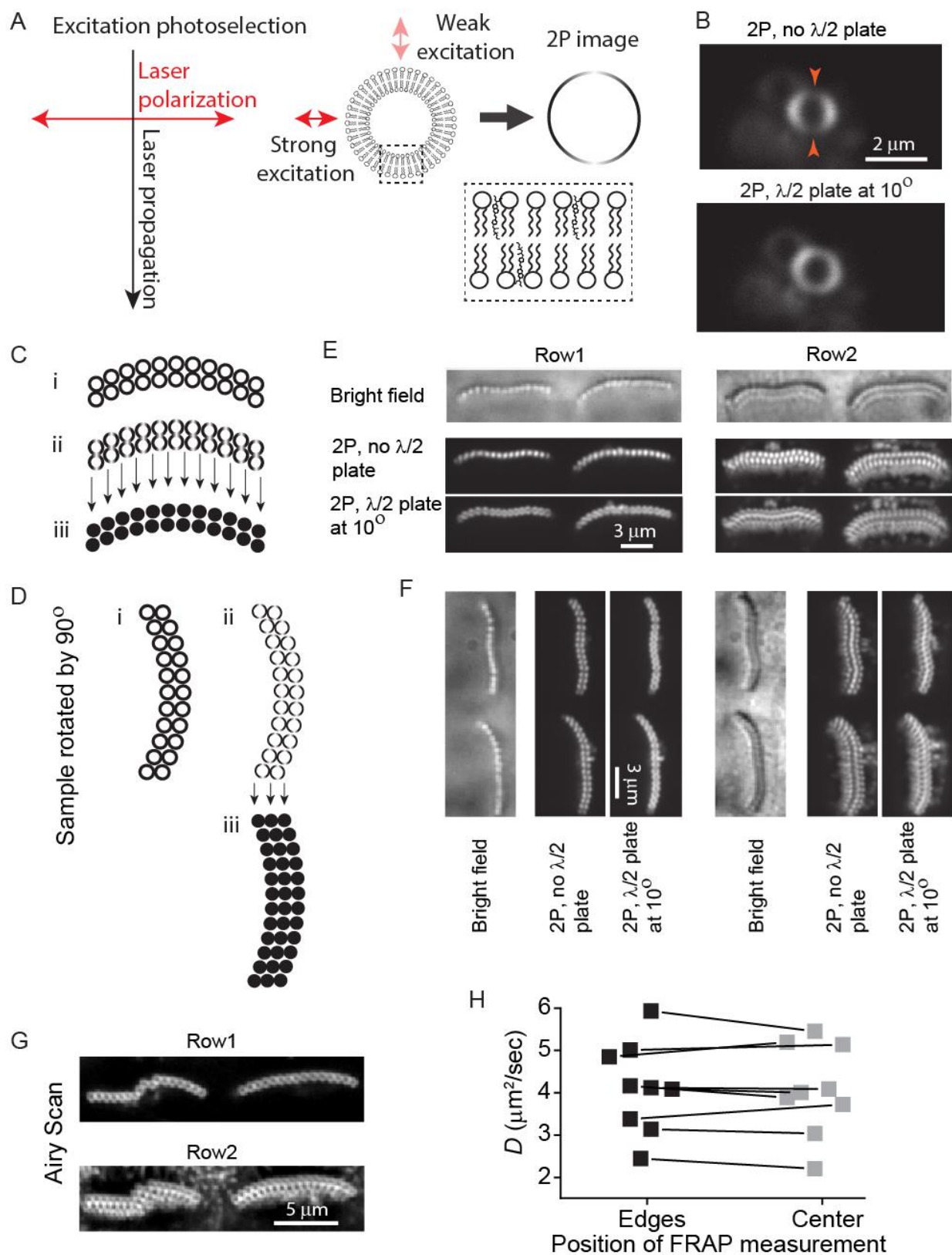
Figure S3. Excitation photoselection. Related to Figure 1. (A) Schematic representation
of excitation photoselection. The inset shows the relative position of di-3-ANEPPDHQ in
the membrane. (B) Two-photon images of a pure DOPC vesicle stained with di-3-

44 ANEPPDHQ without a λ/2 plate (*top*) showing the photoselection effect (orange
45 arrowheads) and with a λ/2 plate at 10° (*bottom*) where the photoselection effect is
46 reduced. (C) Schematic illustration of excitation photoselection effect on a stereociliary
47 row when the laser polarization plane is approximately parallel to the row. In this case,
48 adjacent edges of two stereocilia appear as a filled circle, as do strongly excited
49 semicircular regions without a neighbor, resulting in the number of filled circles in the two-
50 photon image (C iii) being greater than the actual number of stereocilia (C i) by 1. (D)
51 When the rows are perpendicular to the laser polarization, the photoselection effect results
52 in an extra row of filled circles in the two-photon image (D iii). (E) and (F) Bright field and
53 two-photon images with the focus plane at the top of row1 (*left panels*) or row2 (*right
54 panels*). The rows are either parallel (E) or perpendicular (F) to the laser polarization. The
55 excitation photoselection effect results in adjacent stereociliary membranes and strongly
56 excited semicircular regions without neighbors to appear as filled circles (2nd panels). With
57 the λ/2 plate at 10° in the laser path, the photoselection effect is reduced and the
58 stereociliary membranes appear as unfilled circles (3rd panels). (G) Airy scan confocal
59 images of the hair bundle stained with di-3-ANEPPDHQ focusing on the row1 (*top panel*)
60 and row2 (*bottom panel*) stereocilia excited at 480 nm showing no photoselection effect.
61 (H) Comparing the diffusion constant *D* measured at the bright center of a filled circle,
62 which represents the edges of two adjacent stereocilia, to that of the darker region
63 between two filled circles, which represents the center of a stereocilium.
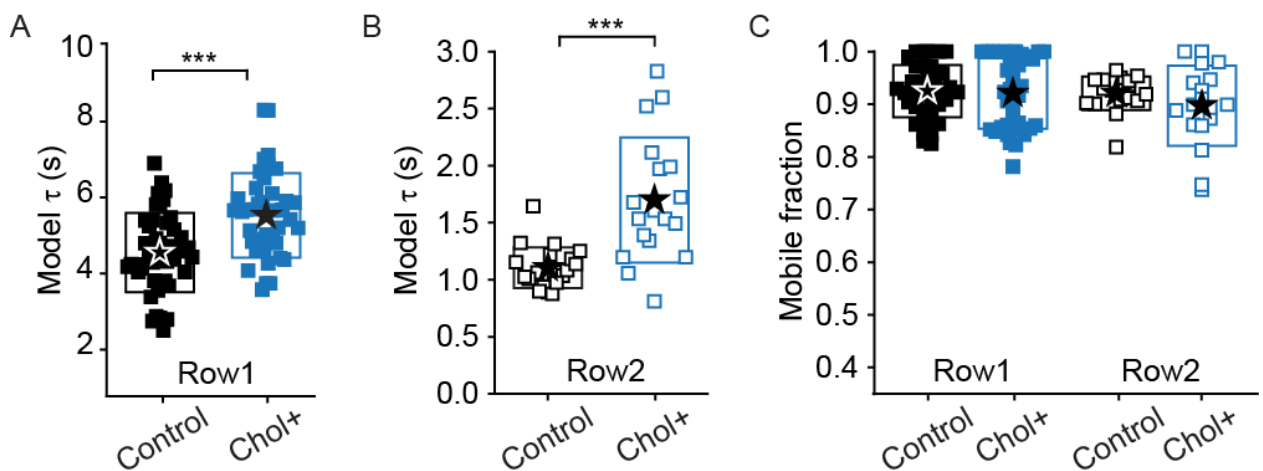
64

65 **Figure S4. Cholesterol loading results in slower recovery.** Related to Figure 1. The
66 time constants τ derived from the Fourier series solutions, showing significantly slower
67 recovery after cholesterol addition in (A) row1 and (B) row2 stereocilia. (C) The mobile
68 fraction of dye is the same after cholesterol addition in both stereocilia rows. Boxes

69   represent SDs and the star symbol indicates the mean. Each data point is a stereocilium.

70   *** $p < 0.001$.

71
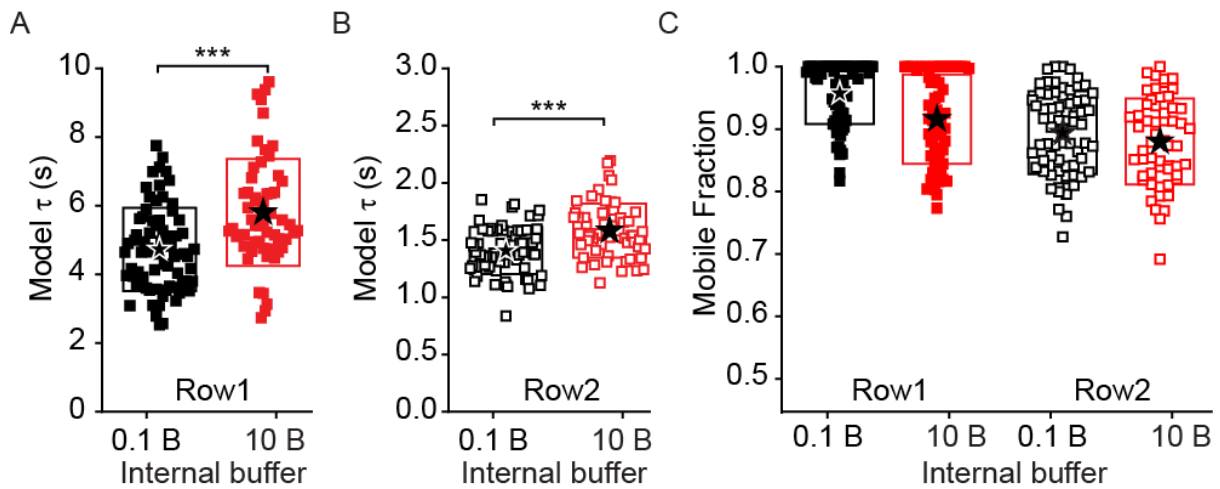
72   **Figure S5. Internal Ca^{2+} results in slower recovery.** Related to Figure 2. (A), (B) The

73   time constants τ showing significantly slower recovery with 10 mM BAPTA internal solution

74   compared to 0.1 mM BAPTA internal solution in (A) row1 and (B) row2 stereocilia. (C)

75   Summary plot of the mobile fraction showing no significant difference between 0.1 and 10

76   mM BATPTA internal solutions in both stereocilia rows. Boxes represent the SDs and the

77   star symbol indicates the mean. Each data point is a stereocilium. 0.1 B = 0.1 mM BAPTA,

78   10 B = 10 mM BAPTA. *** $p < 0.001$.

79
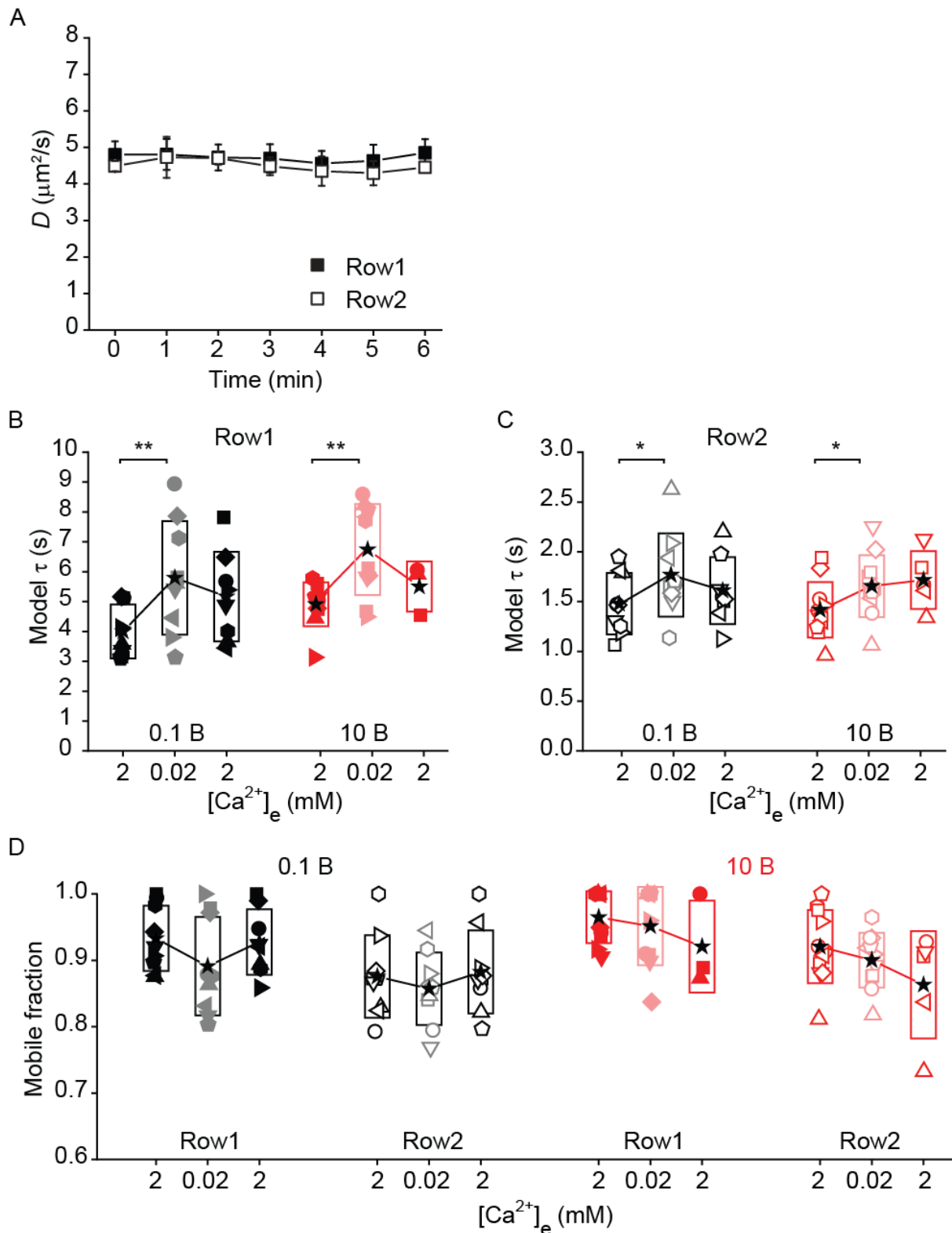
Figure S6. Lowering external Ca²⁺ results in slower recovery. Related to Figure 3. (A) *D* values (mean ± SD) extracted from FRAP measurements repeated over time on different stereocilia within a bundle for both stereocilia rows (n = 11 for row1, n = 8 for row2) show no significant change with time. (B), (C) Summary box plots of time constant τ show a

84 significant reduction in the presence of 0.02 mM Ca^{2+} for both 0.1 mM BAPTA and 10 mM

85 BAPTA internals in (B) row1 and (C) row2 stereocilia. (D) Summary plot of the mobile

86 fraction showing no significant difference between 2 and 0.02 mM external Ca^{2+} in both

87 stereocilia rows irrespective of the internal solution. Boxes represent the SDs and the star

88 symbol indicates the mean. Each colored symbol corresponds to stereocilia from a cell.

89 0.1 B = 0.1 mM BAPTA, 10 B = 10 mM BAPTA. * $p < 0.05$, ** $p < 0.01$, *** $p < 0.001$.
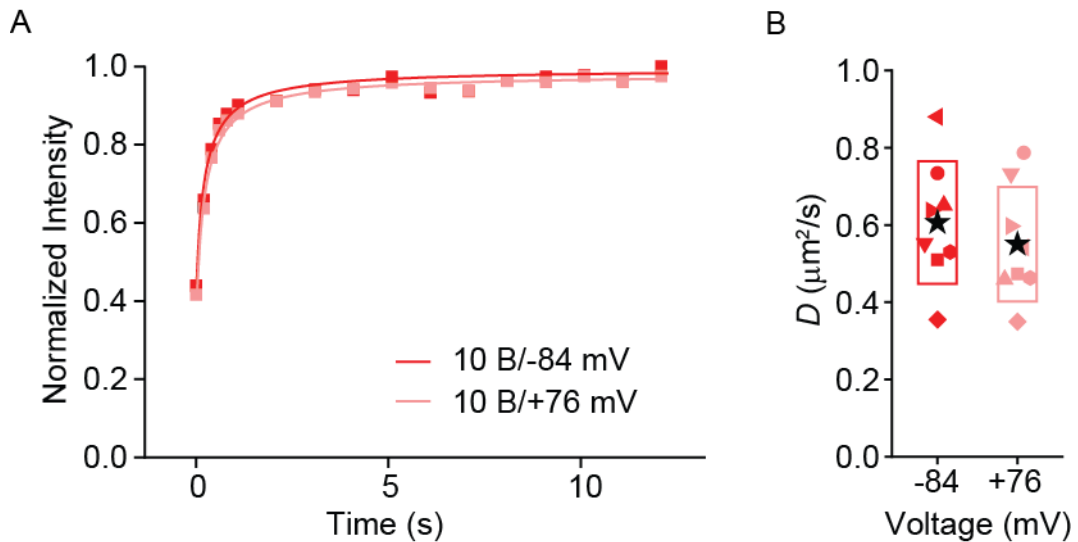
90

91 **Figure S7. Depolarization has no effect on soma FRAP recovery.** Related to Figure 5.

92 (A) Average late FRAP curves from the soma with fitted two-dimensional diffusion model

93 show no change with prolonged depolarization to +76 mV compared to that of -84 mV with

94 10 mM BAPTA internal. Each data point is the mean (n = 8) (B) Summary of diffusion

95 constants from the soma shows no significant difference between the measurements at -

96 84 mV and late depolarization to +76 mV. Different symbols correspond to different cells.

97 Boxes represent the SDs and the black star symbol indicates the mean. 10 B = 10 mM

98 BAPTA.

99   **TRANSPARENT METHODS**

100   **Sample Preparation**

101   *Cochlear Explants:* Sprague Dawley rats of both sexes were sacrificed by decapitation

102   using methods approved by the Stanford University Administration Panel on Laboratory

103   Animal Care. The apical turn of isolated organ of Corti was dissected from pups at

104   postnatal day 8 (P8) to P9 and placed in a recording chamber (Beurg et al., 2009).

105   Dissections were done in extracellular solution containing (in mM): 142 NaCl, 2 KCl, 2

106   $CaCl_2$, 1 $MgCl_2$, 10 HEPES, 6 Glucose, 2 Ascorbate /Pyruvate, 2 Creatine monohydrate,

107   at pH 7.4 and a final osmolality of 304 - 307 mOsm. After removing the tectorial membrane,

108   the tissue was incubated with 6 µM of di-3-ANEPPDHQ (D36801, ThermoFisher Scientific)

109   at room temperature for 5 mins. The tissue was then transferred to the recording chamber

110   with dye-free extracellular solution and held in place with single strands of dental floss

111   while ensuring that IHC bundles were oriented vertically (Ricci and Fettiplace, 1997).

112   During the experiment, tissue was perfused with extracellular solution at rate of 0.3 ml/min

113   maintained at room temperature (19 - 22°C). In addition, extracellular solution was

114   delivered locally to the hair bundle through an apical pipette of tip size ~200 µm (Peng et

115   al., 2016) to wash away any internal solution that might flow from the recording pipette

116   prior to seal formation, without stimulating the hair bundle. For experiments with only

117   electrophysiological recordings, the tissue was not stained with di-3-ANEPPDHQ. No

118   differences were observed in MET properties between cells that were exposed and were

119   not exposed to the dye.

120   *Liposome preparation*: Artificial lipid vesicles were used as a control for testing dye

121   properties as well as the optical system. Liposomes were prepared with 100% 1,2-dioleoyl-

122   sn-glycero-3-phosphocholine (DOPC, Avanti Polar Lipids) on the day of the experiment.

123   The solvent of a 0.1 ml aliquot of 10 mg/ml DOPC in chloroform was evaporated to leave

124   a dried lipid film. Dried lipids were hydrated in 0.25 ml of 100 mM KCl, 10 mM HEPES, pH

125   7.4 for an hour. The lipid solution was then extruded (Mini Extruder, Avanti Polar Lipids)

126   through a 200 nm polycarbonate membrane 11 times. Di-3-ANEPPDHQ was added to the

127   lipid solution in 1:1000 ratio and kept at 4°C, protected from light. For imaging, the

128   liposomes were mounted on a slide in 0.5% agarose gel (Fisher Scientific) to keep them

129   mechanically stable.

130   **Dye Selection and Preparation**

131   Di-3-ANEPPDHQ is a potentiometric lipophilic dye that specifically labels cell membranes

132   including the stereociliary membrane. Di-3-ANEPPDHQ, a chimeric product of di-8-

133   ANEPPS and RH795, was selected over di-8-ANEPPS (a commonly used lipid dye)

134   because it was easier to stain the organ of Corti due to its higher water solubility and it

135   provided a larger fluorescence signal, consistent with previous reports (Obaid et al., 2004).

136   Note that the greater water solubility of di-3-ANEPPDHQ over di-8-ANEPPS may alter

137   lateral membrane diffusion through one or both of two possible mechanisms: 1) A faster

138   return of the bleached dye molecules into the bathing media would produce a larger

139   concentration gradient driving the fluorescent dye into the bleached region. 2) Increasing

140   the rate that unbleached dye returns to the bathing media would make it available for return

141   into the unbleached region, increasing the small portion of FRAP that results from out of

142   plane diffusion.

143   RH795, another lipid dye, was also tested and produced fluorescence recoveries that

144   were in general faster than the di-3-ANEPPDHQ, similar to that described by (Boutet De

145   Monvel et al., 2006). Using di-3-ANEPPDHQ in our study allowed direct comparisons to

146   other published work and the slower time course ensured that we were not under-sampling

147   in our imaging. Although potentiometric, di-3-ANEPPDHQ sensitivity to voltage is limited

148 (Fisher et al., 2008). We tested this by varying membrane potential in recorded hair cells

149 from -84 mV to +76 mV and found no change in the fluorescence signal, supporting the

150 argument that changes in intensity reflects dye diffusion as a measure of lipid properties.

151 Di-3-ANEPPDHQ dye stock solution (30 mM) was prepared in 100% ethanol and stored

152 at -20°C. Working dye solution was made daily by diluting in extracellular solution to a final

153 di-3-ANEPPDHQ concentration of 6 µM in 0.02% ethanol and kept in the dark until used.

154 **Electrophysiology**

155 In most experiments, FRAP was combined with whole-cell voltage clamping to measure

156 MET and membrane diffusivity from the same IHC. Tissue was viewed in brightfield using

157 a fixed-stage upright BX 61WI (Olympus) microscope with a digital Rolera-XR camera

158 (QImaging). Whole-cell patch clamp recordings were obtained using a thick-walled

159 borosilicate patch pipettes (WPI) pulled on a P97 micropipette puller (Sutter Instruments)

160 to 1 - 2 µm inner diameters (3 - 3.5 MΩ). Pipettes were filled with an internal solution

161 containing (in mM): 116 CsCl, 3.5 MgCl$_2$, 3.5 ATP, 5 creatine phosphate, 0.1 Cs$_4$BAPTA,

162 10 HEPES, and 20 ascorbic acid, and with a pH of 7.2 and an osmolality of 285 - 290

163 mOsm. For the 10 mM BAPTA internal solution, CsCl was reduced to balance the increase

164 in BAPTA concentration resulting in the final osmolality of 285 - 290 mOsm.

165   Voltages were adjusted offline for the liquid junction potential and cells were held

166 at -84 mV unless otherwise noted. Elicited currents were low pass filtered at 10 kHz with

167 an Axopatch 200A patch clamp amplifier (Axon Instruments), digitized at 100 kHz using a

168 Personal DAQ3000 (IOtech), and recorded with jClamp (SciSoft). Cells with more than 80

169 pA of leak current (at -84 mV) were discarded. Uncompensated series resistance (Rs) was

170 8.7 ± 1.6 MΩ (n = 196) and the cell capacitance (Cm) was 10.5 ± 1.1 pF (n = 196). After

171 achieving whole-cell mode, cells were allowed to equilibrate for 10-12 minutes to stabilize

172 the resting current, as determined empirically, before beginning FRAP experiments (Ricci

173 and Fettiplace, 1998, Schnee and Ricci, 2003).

174 *Mechanical Stimulation:* Hair bundles were deflected with a custom-built fluid jet system.

175 Thin-walled borosilicate pipettes (10 µm tip diameter) were filled with extracellular solution

176 and positioned across from the hair bundle of interest, within 5 µm. The fluid jet was driven

177 with a 50 Hz sinusoidal wave using a piezo electric disc bender whose input was filtered

178 using an 8-pole Bessel filter (Frequency Devices) at 1 kHz before and then driven by a

179 high voltage/high current amplifier to drive the piezo electric disc.

180 **Drug Delivery**

181 *Cholesterol Loading:* In three tissue preparations, after di-3-ANEPPDHQ staining, the

182 tissue was incubated in 50 mM water-soluble cholesterol (methyl-β-cyclodextrin (mβCD)

183 + cholesterol; Sigma) in extracellular solution for 10 mins before mounting the tissue in the

184 recording chamber with cholesterol-free extracellular solution. This treatment increases

185 the membrane cholesterol in hair cells (Nguyen and Brownell, 1998, Organ and Raphael,

186 2009). FRAP measurements were performed between ~12 and 30 mins after initial

187 exposure to treatment solution.

188 *Low extracellular Ca^{2+}*: The apical perfusion pipette was used to deliver low Ca^{2+}

189 extracellular solution. This solution contained (in mM): 143 NaCl, 2 KCl, 3.3 $CaCl_2$, 4

190 HEDTA, 10 HEPES, and had pH = 7.4 at 304 - 307 mOsm. Free Ca^{2+} concentration was

191 measured using a MI-600 Ca^{2+} electrode (Microelectrodes) calibrated using Ca^{2+} buffer

192 standards (CALBUF-2, WPI) (Ricci and Fettiplace, 1998). The low Ca^{2+} extracellular

193 solution was ~25 - 30 µM free Ca^{2+} (n = 27).

194 *Curare:* The apical perfusion pipette was used to deliver extracellular solution containing

195 1 mM tubocurarine (93750, Sigma) to block MET current.

Two-photon FRAP acquisition

To perform FRAP experiments, we used an Ultima two-photon system (Bruker, formerly Prairie Technologies) coupled with a BX 61WI microscope (Olympus). The excitation source was a Titanium: Sapphire tunable ultrafast Chameleon Ultra II pulsed laser (Coherent). Di-3-ANEPPDHQ was excited at 860 nm and the fluorescence emission was collected through a 100x 1.0 NA water dipping objective lens (Olympus) and redirected to a multi-alkali photo multiplier tube using a 575 nm dichroic filter and a 645/65 nm bandpass filter (Chroma Technologies). For the optical system implemented, the microscope's point spread function (PSF) was calculated using 250 nm fluorescent particles (Spherotech) and the estimated lateral resolution was 0.43 µm and the axial resolution was 1.9 µm.

Each FRAP experiment consisted of a series of time lapse scans of a 2.3 µm by 3.3 µm region that incorporated up to 6 IHC stereocilia; a similar size was used for soma measurements. This region size allowed for a sampling period of 72 msec using a pixel dwell time of 4 µs. During FRAP experiments, the Gaussian laser beam was focused at the top of 5 - 6 stereocilia (Fig. 1A-D). For the soma experiments, the part of the cell membrane slightly above the nucleus was chosen, which allowed separation of the hair cell from the neighboring supporting cell using the patch pipette. The FRAP protocol sequences were as follows: 1) pre-bleach sequence (duration = 5 s, frame rate = 1 fps, laser power at the sample = 1.5 mW), 2) photobleaching pulse (duration = 100 ms, laser power at the sample = 7 mW), and 3) post-bleach sequence (duration = 12 to 20 s, frame rate for first 1 s = 5 fps and frame rate for remaining time = 1 fps, laser power at the sample = 1.5 mW). The laser beam passed through a pockels cell (Conoptics) that regulated the laser power sequence required for FRAP.

FRAP parameters: We calibrated laser power and duration of the photobleaching pulse using di-3-ANEPPDHQ stained stereocilia. Excitation saturation can substantially increase

221 the size of the effective photobleaching PSF (Braeckmans et al., 2006, Mazza et al., 2008)

222 and leads to higher order triplet states, thus affecting the photobleaching mechanism and

223 the reaction order (Loren et al., 2015). A photobleaching power of ~7 mW at the sample

224 was selected, by plotting the normalized fluorescence intensity as a function of laser

225 power, to avoid excitation saturation (Fig. S1A). To allow for rapid photobleaching, we

226 used a bleach duration of 100 ms that achieves 60 to 70 % photobleaching (Fig. S1B).

227 The 100 ms bleach time is short in comparison to the characteristic diffusion time (>1 sec)

228 observed in either the stereocilia or the soma (Fig. 1G) and therefore it is reasonable to

229 assume minimal diffusion during the photobleaching time. To ensure that photobleaching

230 of di-3-ANEPPDHQ was irreversible, DOPC vesicles of size < 0.5 μm were selected that

231 would be completely bleached following our bleaching parameters (Fig. S1C). Our

232 selected parameters demonstrate irreversible bleaching over 12 seconds of fluorescence

233 recording (Fig. S1D). A monitoring power of ~1.5 mW was selected empirically to reduce

234 photobleaching during the monitoring/recovery phase to < 5%.

235 **FRAP curve generation from image data**

236 The time series images were analyzed offline using ImageJ software (NIH) to quantify

237 fluorescence intensities. We measured the average fluorescence intensity of all regions of

238 interest (ROI): the bleached region (BL), a reference region (REF) and a background

239 region (BK) as illustrated in fig. 1C. A custom code implemented in Igor Pro (Wavemetrics)

240 was then used to generate a FRAP curve with normalized fluorescence intensity on the y-

241 axis and time on the x-axis. First, the average background intensity (I_{BK}) was subtracted

242 from the average fluorescence intensity within the bleached spot (I_{BL}) and the reference

243 region (I_{REF}). Next, the background-subtracted intensity values at each time point were

244 normalized to the pre-bleached intensity averaged from the first 5 images just preceding

245 the photobleaching, such that average pre-bleach intensity is set to 1.

$$246 \qquad\qquad I_{BL_{norm}}(t) = \frac{I_{BL}(t) - I_{BK}(t)}{I_{BL\_Prebleach}}$$

$$247 \qquad\qquad I_{REF_{norm}}(t) = \frac{I_{REF}(t) - I_{BK}(t)}{I_{REF\_Prebleach}}$$

248   To account for the limited bleaching that occurs during recovery, the normalized intensity

249   from the bleached ROI ($I_{BL_{norm}}$) is then normalized to the intensity from the reference ROI

250   ($I_{REF_{norm}}$) at each time point to generate the FRAP curve as given below:

$$251 \qquad\qquad I_{FRAP\ curve}(t) = \frac{I_{BL_{norm}}(t)}{I_{REF_{norm}}(t)}$$

252   Plots of time, where t = 0 is the first post bleach measurement, against the normalized

253   intensity are presented for each condition and diffusion constants D are extracted.

254   **FRAP model for diffusion in the stereociliary membrane**

255   To calculate the diffusion constant D, we followed the pure-diffusion model from Axelrod

256   et al. (1976) (detailed in Appendix A). Briefly, we first used a Fourier series (Model 1) for

257   a first approximation of diffusivity D. For the stereocilia, the significant diffusion is axial, i.e.

258   one-dimensional (1D) as in Fig. 1D. As the bleach spot is at the tip of the stereocilia, there

259   is zero flux at the tip with a fluorophore pool at the base. The initial extent of bleaching and

260   the stereocilia length were measured from the live tissue preparation (Fig. S2B, C), which

261   leaves the theoretical recovery with only two parameters – diffusivity D and the long-time

262   limit $F(\infty)$ which is the fluorescence intensity as time approaches ∞. These were

263   determined by a best fit to the measured recovery, using 'NonlinearModelFit' in

264   *Mathematica*.

265   Since the base of the stereocilium is hardly a fluorophore pool as assumed in Model

266   1, we then used Model 2 for a more realistic determination of the diffusivity D. The long-

267   time limit $F(\infty)$ determined from the Model 1 was used in Model 2. Model 2 consisted of a

268   cylindrical body with a tapered rootlet area flaring into a flat plate representing the cuticular

269   plate, with the fluorophore pool placed at the edge of the cuticular plate (Fig. S2A). The

270   diffusion equation remained 1D but required a numerical solution with 'NDSolveValue' in

271   *Mathematica*. The percentage of molecules contributing to the fluorescence recovery

272   termed as "mobile fraction" of recovery f was estimated from the limit $F(\infty)$. The

273   numerical solution for Model 2 yielded an improved value for D that provides a least-square

274   fit of the simulation to the experimental FRAP data (Fig. 1E). The model parameters (D, τ

275   and f) reported in the present study were determined by Model 2, unless stated otherwise.

FRAP model for diffusion in the basolateral membrane

277   To estimate the diffusivity of the soma, we considered the case of uniform lipid-bilayer

278   properties with orthotropic diffusivity in 2D (detailed in Appendix B). The circumferential

279   diffusion is even more important for the present bleaching, which has the small lateral

280   extent of 0.8 µm and an axial extent of 2.2 µm. A double Fourier series is used for a

281   cylindrical surface that represents the basolateral membrane of the IHC. The series is

282   chosen to satisfy the condition of continuity in the circumferential direction and fluorophore

283   pools at the ends in the axial direction. The bleach is a small rectangular region with

284   Gaussian distributions in the *x*- and *y*- directions. Orthotropic diffusivity is included, with

285   different values D_x and D_y in the x- and *y*- directions. However, principal axes of diffusion

286   in off-axis directions is not considered. Our calculations indicate that the orthotropic values

287   cannot be consistently obtained from a single recovery measurement. A second

288   measurement is needed, such as the two-stripe bleaching or recovery from a second point

289   as used in (Boutet De Monvel et al., 2006). However, they find that the ratio of the

290   maximum and minimum diffusivities is generally a factor of only 2, and that the assumption

291   of isotropy yields a diffusivity that is the average. So, we use isotropy $D_x = D_y$, but

292   accurately model the bleach. The result for the theoretical recovery has only two free

293 parameters – the diffusivity D and the limit $F(\infty)$. *Mathematica* with 'NDSolveValue' yields

294 the parameters for a best fit to the experimental recovery in short time. Considering the

295 difference in procedure and analysis, the agreement of our diffusion calculations with

296 (Boutet De Monvel et al., 2006) for the IHC is remarkable (Table S1) considering the

297 recovery curves are so much different (Fig. S2E).

298 **Initial axial extent of bleaching**

299 The initial bleach extent along the stereocilia and soma, and the length of the live

300 stereocilia are critical model parameters. We measured the initial bleach extent in z-axis

301 by bleaching the stereocilium tip and acquiring fast z-stacks (15 ms frame period) using a

302 250 µm Z-axis Piezo Drive (Bruker) along the stereocilium length immediately after

303 bleaching. Measurements were taken for both stereociliary rows oriented either standing

304 up almost vertically (<10°) or at an angle >10°, and for the basolateral membrane (Fig.

305 S2B). The degree of bleaching along the z-stack was normalized to that at the plane of

306 bleaching and then plotted against the position along the z-axis relative to the bleach spot.

307 Gaussian fitting was used to measure the effective axial extent of bleaching (Fig. S2B).

308 The initial axial extent of bleaching (i.e., half width of full wave half maximum (FWHM)

309 derived from the gaussian fitting) was dependent on the orientation of the row 1 stereocilia

310 which were measured (mean ± SE) as 1.35 ± 0.06 µm (n = 19) and 0.95 ± 0.07 µm (n =

311 17) for standing up and angled orientations respectively. The row 2 stereocilia was

312 measured to be 1.84 ± 0.3 µm (n = 21) for both orientations. For the basolateral membrane,

313 the initial bleach axial extent was measured as 1.1 ± 0.1 µm (n = 10), slightly higher than

314 the theoretical value of 0.9 µm estimated for the two-photon excitation wavelength of 860

315 nm and objective NA of 1.0.

316 The observed larger axial extent of bleaching in the row 2 stereocilia could be potentially

317 due to the reflection or scattering of high-power laser (Zezell and Ana, 2015) from the

318   neighboring row 1 stereocilia and the cuticular plate resulting in extended bleaching. These

319   data illustrate the importance of calibrating each component being investigated (row 1, 2

320   and soma) as we estimate a potential diffusion coefficient errors of up to 30% for a single

321   point calibration that could inadvertently suggest differences between stereociliary rows.

322   The diffusion constants reported in the present study were determined using the values

323   1.35 μm and 1.84 μm for row 1 and row 2 stereocilia respectively as the bundles were

324   oriented vertically.

325   **Stereocilia length**

326   For an accurate estimation of the stereocilia length, the tissue was incubated in 6 μM di-

327   3-ANEPPDHQ and mounted in a recording chamber. Live-cell z-stack images of the hair

328   bundle were taken in Airy-scan mode under LSM 880 confocal microscope (Zeiss) with a

329   water immersion 40x 1.0 NA objective (Zeiss), followed by 3D reconstruction of the hair

330   bundle using Imaris 9.3.1 (Oxford Instruments).

331   Stereocilia lengths were estimated as 6.6 ± 0.2 μm (n = 56 stereocilia from 3 animals) for

332   row 1 and 3.0 ± 0.2 μm (n = 17 stereocilia from 3 animals) for row 2 (Fig. S2C). Given that

333   stereocilia length is an important parameter, we estimated the diffusion coefficient D for

334   lengths ± 2 standard deviation of the sample (SD) from the mean stereocilia lengths. We

335   found that the 2 SD change in the stereocilia length resulted in a 3% and 11% change in

336   the estimated diffusion constant for row 1 and row 2 respectively (Fig. S2D).

337   **Excitation Photoselection**

338   As di-3-ANEPPDHQ is a lipophilic dye that fluoresces only in the presence of lipid, the

339   two-photon microscopy images of individual stereocilia membrane were expected to

340   appear as unfilled circles. However, in the present study, each row of stereocilia appeared

341   as a collection of filled circles with brighter fluorescence intensity in the center of each

342   circle (Fig. 1B, C). To accurately monitor diffusion within the membrane, dye must only be

343   present in the membrane as replenishment must be from diffusion within the membrane

344   and not entry from extracellular or intracellular fluid. The filled appearance of stereocilia

345   was potentially a problem as it suggested there was dye in the cytoplasm. However, we

346   determined that the observed fluorescence pattern was an artefact due to the orientation

347   of the dye in the stereociliary membrane and the polarization of the excitation laser

348   resulting in the *excitation photoselection effect* as illustrated in Fig. S3A. The

349   *photoselection effect* arises when the fluorophore molecules having transition dipole

350   moments aligned parallel to the plane of polarization of the excitation laser are strongly

351   excited, whereas the fluorophore molecules that are aligned perpendicular to the excitation

352   polarization are weakly excited (Parasassi et al., 1997, Bagatolli, 2006). This results in

353   each stereocilium appearing as two semicircles instead of a circle as illustrated by the di-

354   3-ANEPPDHQ stained DOPC vesicles (Fig. S3B). When a stereociliary row is aligned

355   parallel to the laser polarization, adjacent semicircles of neighboring stereocilia from the

356   same row appear to be a single filled circle, as do strongly excited semicircular regions

357   without a neighbor (Fig. S3C, E). Thus, each row of stereocilia had an extra filled circle

358   compared to the actual number of stereocilia. In the case of rows perpendicular to the

359   laser polarization, two adjacent crescents from the neighboring rows form a filled circle, as

360   do isolated crescents, resulting in an apparent additional row of filled stereocilia, one more

361   than the actual number of stereociliary rows (Fig. S3D, F). We confirmed and corrected

362   for the *photoselection effect* by rotating the laser polarization with a λ/2 (half-wave) plate,

363   thus converting filled stereocilia to unfilled stereocilia (Fig. S3E, F). Note the excitation

364   photoselection effect was not visible with confocal imaging (Fig. S3G). No difference was

365   found in FRAP recovery with or without the λ/2 plate rotation and most importantly,

366   diffusion was only occurring through the membrane ((paired *t-test*, $p > 0.05$, Fig. S3H).

367 **Data Analysis**

368 We used Mathematica 12.0 to fit the experimental FRAP data when estimating the

369 diffusion parameters. Whole cell currents were visualized and analyzed using jClamp

370 (SciSoft) and OriginPro 2018 (OriginLabs). Graphs were generated with OriginPro 2018

371 (OriginLabs) and Adobe Illustrator CS6 (Adobe). All statistical analyses used two-sample

372 Student's t test performed using OriginPro 2018 (OriginLabs). All *p* values presented used

373 paired t tests with comparisons within a cell, and unpaired unequal variance tests across

374 cell conditions. Significance (*p* values) are * $p < 0.05$, ** $p < 0.01$, *** $p < 0.001$. Data are

375 presented as mean and standard deviation of the sample (SD), unless stated otherwise.

376 **Appendix A: One-dimensional diffusion model for cylindrical stereocilia**

377 Following (Axelrod et al.), it is presumed the bleaching of di-3-ANEPPDHQ is a simple

378 irreversible first-order reaction, and that our bleaching time of 100 ms is short in

379 comparison to the characteristic diffusion time (1 - 4 sec) and henceforth there is minimal

380 diffusion during the bleaching time. The movement of fluorophores within the stereociliary

381 membrane after bleaching is modeled to be 1D along the length of the stereocilium.

382 *Diffusion equation for simple cylinder*

383 We approximate the plasma membrane of the stereocilium by a straight cylinder. The post-

384 bleach concentration of fluorophores is

$$C(x,t) = C_0 - B(x,t) \tag{1}$$

386 where C_0 is the uniform concentration of pre-bleach fluorophores and $B(x,t)$ is the

387 concentration of bleached fluorophores at position x from the tip of the stereocilium and

388 time t. The latter can be separated into a volume fraction *f* that diffuses and a portion $(1 -$

389 *f*) that is immobile:

$$C(x,t) = C_0 - B(x,0)(1-f) - fB(0,0)\tilde{B}(x,t) \tag{2}$$

391   in which the normalized mobile bleach concentration $\tilde{B}(x,t)$ satisfies the conditions:

392
$$\tilde{B}(x,0) = B(x,0)/B(0,0) \tag{3}$$

393
$$\tilde{B}(x,\infty) = 0 \tag{4}$$

394   and satisfies the simple 1D diffusion equation,

395
$$\frac{\partial \tilde{B}(x,t)}{\partial t} = D \frac{\partial^2 \tilde{B}(x,t)}{\partial x^2} \tag{5}$$

396   where D is the diffusion coefficient. We use a Gaussian distribution for the initial bleach

397   intensity

398
$$I(x) = e^{-x^2/2w^2} \tag{6}$$

399   in which the half width of FWHM $x_{1/2}$ is related to w:

400
$$x_{1/2} = w\sqrt{2 \log 2} = 1.177w \tag{7}$$

401   The observed fluorescence recovery, normalized to the prebleach value is:

402
$$F(t) = \frac{\int_0^{L_0} I(x)C(x,t)dx}{\int_0^{L_0} I(x)C_0 dx} \tag{8}$$

403   The fluorescence is integrated from the tip to the distance L_0. This can be written as:

404
$$F(t) = F(\infty) - [F(\infty) - F(0)]A(t) \tag{9}$$

405   where the mobile bleach is in the term:

406
$$A(t) = \frac{\int_0^{L_0} I(x)\tilde{B}(x,t)dx}{\int_0^{L_0} I(x)\tilde{B}(x,0)dx} \tag{10}$$

407   Since $\tilde{B}(x,\infty) = 0$, so that $A(\infty) = 0$, the observed long-time limit $F(\infty)$ is the

408   fluorescence intensity as t approaches ∞, and $F(0)$ is the measured value immediately

409   post-bleach. If the fraction of mobile fluorophores f is made explicit, the recovery is:

410
$$F(t) = (1-f)F(0) + f\left[1 - \left(1 - F(0)\right)A(t)\right] \tag{11}$$

411   Therefore, the observed limit is related to the fraction by the relation:

$$412 \qquad\qquad f = \frac{F(\infty) - F(0)}{1 - F(0)} \qquad\qquad (12)$$

413   The initial post-bleach distribution $\tilde{B}(x, 0)$ is normalized to the value 1 at the tip and shown

414   in Fig. S2B. This can be approximated by the intensity:

$$415 \qquad\qquad \tilde{B}(x, 0) \sim I(x) \qquad\qquad (13)$$

416   This is valid when the bleach parameter K in Axelrod, et al. 1976 is around 1, which is the

417   present case. As the bleach spot is at the tip of the stereocilia, the tip has zero flux,

418   $\partial \tilde{B}(0, t)/\partial x = 0$, and there is a lipid pool at the cuticular plate at x = L, i.e., $\tilde{B}(L, t) = 0$.

419   With these initial and boundary conditions, the solution of the diffusion equation (Eq. 5) is

420   unique and depends only on the diffusivity D. Consequently, the recovery Eq. 9 has only

421   two free parameters, the long-time limit $F(\infty)$ and the diffusivity D, which are determined

422   from a fit to the measured recovery.

423   *Fourier series solution to diffusion equation, Model 1*

424   The solution to Eq. 5 satisfying the given boundary conditions and the initial condition given

425   by Eq. 13 can be given by a Fourier series in the spatial coordinates:

$$426 \qquad\qquad B(x, t) = \sum_{n=1}^{\infty} B_n e^{-\frac{t}{t_n}} Cos \frac{(2*n-1)\pi x}{2L} \qquad\qquad (14)$$

427   in which the time constants $t_n = \frac{1}{D} \left[\frac{2L}{(2n-1)\pi} \right]^2$, so that successive time constants become

428   small i.e., $t_2 = \frac{1}{9} t_1$, $t_3 = \frac{1}{25} t_1$, $t_4 = \frac{1}{49} t_1$ etc. A similar 1D Fourier series is used by Organ

429   and Raphael (2009) for the cell body with a lipid pool at both ends. With Mathematica, Eq.

430   9 is used directly in "NonlinearModelFit" to obtain a least-squares fit of the experimental

431   FRAP curve, yielding the diffusivity D and the limit $F(\infty)$. The time constant τ is used to

432   characterize the recovery curve, which is the time at which the mobile recovery is at

433   midpoint:

$$F(\tau) = \frac{1}{2}[F(\infty) - F(0)] \qquad (15)$$

435   This τ is a combination of the time constants in Eq. 14 and is determined numerically from

436   the least squares fit.

437   *More realistic geometry model, Model 2*

438   The drawback of the Fourier series solution is the lipid pool at the base of the stereocilium.

439   A direct numerical solution is better in that various effects can be included. So, we used a

440   more realistic geometry which consists of a straight stereocilium with a tapered root,

441   attached to the cuticular plate, and a lipid pool at the edge of the cuticular plate (Fig. S2A).

442   This remains an axisymmetric problem, but s the arc length along the meridian must be

443   used instead of the axial coordinate x. The diffusion equation is now:

$$\frac{\partial \tilde{B}(s,t)}{\partial t} = D\left(\frac{\partial^2 \tilde{B}(s,t)}{\partial s^2} + \frac{dr(s)}{r(s)ds}\frac{\partial \tilde{B}(s,t)}{\partial s}\right) \qquad (16)$$

445   where $r(s)$ is the radial distance from axis to surface. Calculations show that the details of

446   the end have some effect on the recovery, but the exact radius of the cuticular plate and

447   edge condition, pool or zero flux, have little effect.

448   A comparison between the models showed that Model 1 with Fourier series solution Eq.

449   14 produce similar recovery curves to that of Model 2 if the length used in Model 1 was

450   increased by 10%; the extra length simulates the effect of the cuticular plate. The

451   procedure was to use Model 1 with the effective length (i.e., 10% longer than the estimated

452   stereocilia length) for a fast determination of the limit $F(\infty)$ and a first approximation for

453   the value of D that minimizes the difference in the numerical solution and the

454 measurement. Then, we used the numerical solution for Model 2 (Fig. S2A) using the

455 stereocilia length estimated from the live tissue preparation (see below for details) that

456 yielded an improved value for D that provides a least-squares fit of the simulation to the

457 experimental FRAP data as shown in Fig. 1E.

458 Boutet De Monvel et al. (2006) measured the bundle of outer hair cell (OHC) stereocilia

459 with a 2D analysis and obtained D in the range 0.7 – 1.1 μm^2/s for the axial direction and

460 the much slower values of 0.16 – 0.3 μm^2/s in the perpendicular direction. So, our

461 neglect of the circumferential diffusion seems justified. Our results for the rat IHC

462 stereocilia in the axial direction are higher with $D \sim 5$ μm^2/s (Fig. 1H).

463 **Appendix B: Two-dimensional diffusion model for soma**

464 For local bleaching of the soma, the diffusion in the lipid bilayer is two dimensional. Boutet

465 De Monvel et al. (2006) considered orthotropy of the diffusion in the wall of the OHC. They

466 use two stripes of bleaching as well as the usual spot bleaching with monitoring of recovery

467 at a second region to obtain the necessary information to discriminate between the

468 diffusion in the axial and circumferential directions. The axial diffusivity is about twice the

469 circumferential. Of interest is that the principal axes of diffusivity seem to align with the

470 cytoskeleton. In Chen and Zhao (2007), the bleach is a circular spot, and the diffusivity is

471 assumed to be isotropic. The Gaussian spot in an infinite domain has a simple

472 approximation for the recovery, which they use to find that for the OHC, $D \sim 0.2$ μm^2/s,

473 similar to the 0.3 μm^2/s found by Boutet De Monvel et al. (2006). Organ and Raphael

474 (2009) also use a spot bleach, but in the analysis use a 1D Fourier series for the diffusion

475 in the axial direction and neglect the diffusion in the circumferential direction.

476 Consequently, their result of $D \sim 1.67$ μm^2/s is an order of magnitude higher.

477 The diffusion in the circumferential direction is even more important in our measurements,

478 since the width of intensity in the circumferential direction is narrower than in the axial

479   direction. We consider the case of constant properties of the bilayer with orthotropic

480   diffusivity, so the equation for the concentration of bleached lipids is the diffusion equation

481   in the form:

482
$$\frac{\partial \tilde{B}(x,y,t)}{\partial t} = D_x \frac{\partial^2 \tilde{B}(x,y,t)}{\partial x^2} + D_y \frac{\partial^2 \tilde{B}(x,y,t)}{\partial y^2} \tag{17}$$

483   The surface is taken as cylindrical with the coordinates consisting of the circumferential

484   distance y and the axial distance x. The diffusivities in the x- and y- directions are D_x and

485   D_y, i.e., the orthotropic axes are in line with the x- and y- directions instead of being

486   skewed as shown by Boutet de Monvel, et. al (2007). The bleach is centered at the point

487    $x = 0$ and $y = 0$. The axial distance to the end of the cell is *a* so the total length is 2*a*, and

488   the circumferential distance to the opposite point is *b*, so the diameter of the cell is 2b/π.

489   The initial bleach is approximated to be Gaussian in both x- and y- directions:

490
$$I(x,y) = e^{-\frac{x^2}{2w_x^2} - \frac{y^2}{2w_y^2}} \tag{18}$$

491   which permits a different distribution in the x- and y- directions. Therefore, the solution of

492   the diffusion equation is sought that satisfies the initial condition:

493
$$\tilde{B}(x,y,0) = I(x,y) \tag{19}$$

494   and the end conditions of a lipid pool:

495
$$\tilde{B}(\pm a, y, 0) = 0 \tag{20}$$

496   and the circumferential condition of continuity:

497
$$\frac{\partial \tilde{B}(x,b,t)}{\partial y} = 0 \tag{21}$$

498   *Fourier series solution to diffusion equation*

499   The differential equation and the boundary conditions are satisfied by a double Fourier

500   series in the form:

$$\tilde{B}(x,y,t) = \sum_0^{N_y} \sum_1^{N_x} B_{mn} e^{-t/t_{mn}} \cos\frac{(2*m-1)\pi x}{2a} \cos\frac{n\pi y}{b} \tag{22}$$

502   where the time constants are:

$$\frac{1}{t_{mn}} = D_x \left[\frac{(2*m-1)\pi}{2a}\right]^2 + D_y \left[\frac{n\pi}{b}\right]^2 \tag{23}$$

504   The number of harmonics used are N_x and N_y in the x- and y- directions. The Fourier

505   coefficients B_{mn} are determined from the initial condition Eq. 19 in the standard procedure.

506   *Recovery calculation*

507   The recovery is measured by integrating the fluorescence over the rectangular region;

$$-L_x < x < L_x, -L_y < y < L_y \tag{24}$$

509   The recovery curve is then:

$$F(t) = F(\infty) + \big(F(\infty) - F(0)\big)A(t) \tag{25}$$

511   where the normalized bleaching is:

$$A(t) = \int_{-L_y}^{L_y}\int_{-L_x}^{L_x} I(x,y)\tilde{B}(x,y,t)dxdy \bigg/ \int_{-L_y}^{L_y}\int_{-L_x}^{L_x} I(x,y)\tilde{B}(x,y,0)dxdy \tag{26}$$

513   The initial post bleach measured value is $F(0)$. If the lengths are known, then there are

514   only three free parameters in this theoretical recovery curve - the diffusivities D_x and D_y

515   and the limit $F(\infty)$. The relation between the mobile fraction and the limit in the recovery is

516   the same Eq. 12. We find that one recovery measurement is not sufficient to discriminate

517 D_x and D_y. Consequently, we use isotropy with $D = D_x = D_y$. It appears that D is the

518 average of the actual values of D_x and D_y.

519 *Curve fits using Mathematica*

520 We consider a cell with length 40 µm and diameter 8 µm and initial bleach width (FWHM)

521 of around 0.8 µm and 2.2 µm in the *x*- and *y*- directions. The theoretical recovery can be

522 written in Mathematica with just the two free parameters D and $F(\infty)$. Then, the command

523 "NonlinearModelFit" determines both parameters for a best fit to the measured recovery

524 curve. A high number of harmonics provides a good approximation to the Gaussian

525 distributions of initial bleach; we find that 40 in each direction is adequate.

526

527 **Supplemental References**

528 Axelrod D, Koppel D, Schlessinger J, Elson E, Webb W 1976. Mobility measurement by
529   analysis of fluorescence photobleaching recovery kinetics. *Biophysical Journal,* 16**,**
530   1055-1069.

531 Bagatolli LA 2006. To see or not to see: Lateral organization of biological membranes
532   and fluorescence microscopy. *Biochimica Et Biophysica Acta-Biomembranes,* 1758**,**
533   1541-1556.

534 Beurg M, Fettiplace R, Nam JH, Ricci AJ 2009. Localization of inner hair cell
535   mechanotransducer channels using high-speed calcium imaging. *Nature neuroscience,*
536   12**,** 553-558.

537 Boutet de Monvel J, Brownell WE, Ulfendahl M 2006. Lateral diffusion anisotropy and
538   membrane lipid/skeleton interaction in outer hair cells. *Biophysical Journal,* 91**,** 364-
539   381.

540 Braeckmans K, Stubbe BG, Remaut K, Demeester J, De Smedt SC 2006. Anomalous
541   photobleaching in fluorescence recovery after photobleaching measurements due to
542   excitation saturation- a case study for fluorescein. *Journal of Biomedical Optics,* 11**,**
543   044013.

544 Chen GD, Zhao HB 2007. Effects of intense noise exposure on the outer hair cell plasma
545   membrane fluidity. *Hearing research,* 226**,** 14-21.

546 Fisher JAN, Barchi JR, Welle CG, Kim GH, Kosterin P, Obaid AL, Yodh AG, Contreras
547   D, Salzberg BM 2008. Two-photon excitation of potentiometric probes enables optical
548   recording of action potentials from mammalian nerve terminals in situ. *Journal of*
549   *Neurophysiology,* 99**,** 1545-1553.

550 Loren N, Hagman J, Jonasson JK, Deschout H, Bernin D, Cella-Zanacchi F, Diaspro A,
551   McNally JG, Ameloot M, Smisdom N, Nyden M, Hermansson AM, Rudemo M,
552   Braeckmans K 2015. Fluorescence recovery after photobleaching in material and life
553   sciences: putting theory into practice. *Quarterly Reviews of Biophysics,* 48**,** 323-387.

554 Mazza D, Braeckmans K, Cella F, Testa I, Vercauteren D, Demeester J, De Smedt SS,
555   Diaspro A 2008. A new FRAP/FRAPa method for three-dimensional diffusion
556   measurements based on multiphoton excitation microscopy. *Biophysical Journal,* 95**,**
557   3457-3469.

558 Nguyen TVN, Brownell WE 1998. Contribution of membrane cholesterol to outer hair cell
559   lateral wall stiffness. *Otolaryngology-Head and Neck Surgery,* 119**,** 14-20.

560   Obaid AL, Loew LM, Wuskell JP, Salzberg BM 2004. Novel naphthylstyryl-pyridinium
561   potentiometric dyes offer advantages for neural network analysis. *Journal of*
562   *Neuroscience Methods,* 134**,** 179-190.
563   Organ LE, Raphael RM 2009. Lipid lateral mobility in cochlear outer hair cells: regional
564   differences and regulation by cholesterol. *J Assoc Res Otolaryngol,* 10**,** 383-396.
565   Parasassi T, Gratton E, Yu WM, Wilson P, Levi M 1997. Two-photon fluorescence
566   microscopy of Laurdan generalized polarization domains in model and natural
567   membranes. *Biophysical Journal,* 72**,** 2413-2429.
568   Peng AW, Gnanasambandam R, Sachs F, Ricci AJ 2016. Adaptation Independent
569   Modulation of Auditory Hair Cell Mechanotransduction Channel Open Probability
570   Implicates a Role for the Lipid Bilayer. *Journal of Neuroscience,* 36**,** 2945-2956.
571   Ricci AJ, Fettiplace R 1997. The effects of calcium buffering and cyclic AMP on
572   mechanoelectrical transduction in turtle auditory hair cells. *Journal of Physiology-*
573   *London,* 501**,** 111-124.
574   Ricci AJ, Fettiplace R 1998. Calcium permeation of the turtle hair cell
575   mechanotransducer channel and its relation to the composition of endolymph. *Journal*
576   *of Physiology-London,* 506**,** 159-173.
577   Schnee M, Ricci A 2003. Biophysical and pharmacological characterization of voltage‐
578   gated calcium currents in turtle auditory hair cells. *The Journal of physiology,* 549**,** 697-
579   717.
580   Zezell DM, Ana PA 2015. High power lasers and their interaction with biological tissues.
581   *Lasers in Dentistry: Guide for Clinical Practice,* 33**,** 11.
582